

Thermally inflated accretors in post-mass transfer binaries: Abell 35 and its class revisited

SOUMYADEEP BHATTACHARJEE ¹, KAREEM EL-BADRY ¹, JIM FULLER ², CHEYANNE SHARIAT ¹ AND
NATSUKO YAMAGUCHI ¹

¹*Department of Astronomy, California Institute of Technology, 1216 E. California Blvd, Pasadena, CA, 91125, USA*

²*TAPIR, Mailcode 350-17, California Institute of Technology, Pasadena, CA 91125*

ABSTRACT

A small but growing class of binaries containing hot ($T_{\text{eff}} \sim 10^5$ K) white dwarfs (WDs) and rapidly rotating, apparently subgiant companions – including the prototype, Abell 35 – show companions that are too large and luminous to be ordinary main-sequence stars yet too numerous to be explained as finely tuned near-twin binaries. We argue that these stars are instead main-sequence accretors temporarily inflated out of thermal equilibrium by recent mass transfer. For the subgiant of Abell 35, a new Gaia DR3 astrometric orbit ($P_{\text{orb}} = 790$ d) combined with updated photometric and spectroscopic constraints yield $T_{\text{eff}} \approx 4900$ K, $R \approx 3 R_{\odot}$, near-solar metallicity, and rapid rotation aligned with the orbit ($v_{\text{rot}} \approx 195$ km s⁻¹), indicating substantial recent accretion and spin-up. Dynamical mass limits disfavor a coeval twin-binary origin, supporting the inflated-accretor interpretation. We test this scenario using self-consistent MESA binary evolution calculations with a new accretion prescription in which accreted material retains a fraction of its infall energy. The accretor expands to giant-like radii when \dot{M} is high yet remains within its Roche lobe, allowing stable mass transfer even for mass ratios traditionally considered unstable. After mass transfer ceases, the star contracts on Myr timescales through a bloated, rapidly rotating phase whose temperatures, radii, and spins match those observed in Abell 35–type systems. This framework explains the population without fine tuning and unifies Abell 35-type binaries with post-AGB binaries, blue lurkers, and wide WD+main-sequence systems as successive stages of the same post–mass-transfer evolutionary pathway.

Keywords: Stellar accretion (1578) – Roche lobe overflow (2155) – Interacting binary stars (801) – Subgiant stars (1646) – White dwarf stars (1799) – Planetary nebulae nuclei (1250)

1. INTRODUCTION

Mass transfer is a crucial phenomenon in binary systems which can dramatically alter the evolution of the stars. In this work, we focus on low mass stars which form white dwarfs (WD). Interaction is most frequently triggered when the more massive star evolves off the main sequence to the giant branches and fills its Roche lobe. Stable mass transfer that begins when the primary is a subgiant (SG) or red giant branch (RGB) star forms hot subdwarfs (e.g. Han et al. 2003), low-mass red giants (e.g. El-Badry et al. 2022; Jayasinghe et al. 2022), and helium white dwarfs (e.g. Sun & Arras 2018; Li et al. 2019). Most binaries formed through this process have orbital periods $\gtrsim 10^2$ days. However, mass transfer from evolved and convective donors often leads to instability and common envelope (CE) evolution (Ivanova et al. 2013). This typically results in short-period ($\lesssim 1$ day) orbits. Short-period WD + main sequences binaries (e.g. Rebassa-

Mansergas et al. 2007; Parsons et al. 2016), cataclysmic variables (e.g. Meyer & Meyer-Hofmeister 1979), and close binaries found inside planetary nebulae (PNe, Bond & Livio 1990; Jones 2020) are usually assumed to have formed via CE evolution.

There is, however, an emerging population of post-interaction binaries which appear to challenge this classical boundary between stable and unstable mass transfer. The binary separations of these systems fall between the predictions of models for CEE and stable mass transfer, with periods of ~ 10 to ~ 1000 days. A handful of such systems were serendipitously discovered in spectroscopic and photometric surveys over the last few decades, including IK Pegasi (Wonnacott et al. 1993) and the Kepler self-lensing binaries (SLBs; Kruse & Agol 2014; Kawahara et al. 2018; Masuda et al. 2019; Yamaguchi et al. 2024a), but a large population of such objects was discovered with astrometric orbits from the Gaia mission (Shahaf et al. 2023; Yamaguchi et al. 2024c,b). Several works have modeled these binaries as having formed via CEE with an asymptotic giant branch (AGB) donor and efficient envelope ejection (e.g. Yamaguchi et al. 2024b; Belloni et al. 2024). But recent studies have increasingly favored

a stable mass transfer origin of these systems (Ge et al. 2020; Temmink et al. 2023; Hallakoun et al. 2024; Yamaguchi et al. 2025), appealing to models in which mass transfer from an AGB donor remains stable over a wider range of mass ratios than classically assumed (e.g. Ge et al. 2020; Temmink et al. 2023).

Mass transfer can have profound effects on the accreting star (henceforth, the accretor), especially when it is stable. The accreted material carries both angular momentum and energy. The former can spin up the accretor to near-critical rotation rates (Packet 1981; Popham & Narayan 1991), such that anomalously rapid rotation in old stars is often a sign of recent accretion (e.g. Leiner et al. 2019; Nine et al. 2023).

The effects of the accretion energy on the accretor are uncertain but may be even more dramatic. Rapid accretion can temporarily throw the accretor out of thermal equilibrium, especially if the accretion timescale is shorter than the thermal timescale of the star. This is predicted to inflate the accretor to potentially orders of magnitude larger radii (Kippenhahn & Meyer-Hofmeister 1977; Neo et al. 1977a; Fujimoto & Iben 1989; Lau et al. 2024). Thus, a main sequence accretor may attain the dimensions of a giant. This may have significant effects on the outcome of the binary interaction. For example, if the inflated accretor fills its own Roche lobe, it can lead to a CE. Thus, it is crucial to study this effect systematically. Observing systems in this phase of inflation is challenging, as the inflated state of the accretor is short lived: soon after the mass transfer stops, the accretor starts contracting back to the main sequence. Additionally, it is difficult to distinguish temporarily inflated accretors from stars that naturally expanded after they terminated their main-sequence evolution.

A natural place to search for inflated accretors is in post-stable mass transfer binaries hosting hot ($T_{\text{eff}} \sim 10^5$ K) young WDs, which must have just recently transferred some of their envelope to their companions. We thus introduce the class of systems which forms the focus of this work: Abell 35 (hereafter, A35) type systems, named after the prototype. The majority of the known systems are inside PNe. These are wide binaries with a hot WD. However, unlike the other systems, the companions are (sub)giants. The subgiants are fast rotating (telltale sign for a recent accretion history), with rotational periods in the range of $\sim 1 - 10$ days. A concise account of these systems can be found in section 8 of Bond & Zeimann (2024). The orbital period in only one of the eight systems¹ have been known from radial velocity studies ($P_{\text{orb}} \approx 2700$ day in PN LoTr 5, Jones et al. 2017). And, in this work, we report the 790 day period of the prototype A35 obtained from Gaia DR3 astrometry solution, making it the second A35-type system with a known period. Three other

systems (and also LoTr 5) have Gaia RUWE > 1.4 which hints at similarly long periods.

The highlight of these systems is the subgiant nature of the companion. It is possible that these are simply evolved stars. Given the young age of the WD, this can only be achieved with a twin binary (where the initial mass ratio is near unity). However, such an initial condition is too fine-tuned to explain the current and growing population of A35-type systems. Additionally, the lack of known main-sequence companions in similar binaries further renders this unlikely.

In this work, we explore the alternate possibility that the companions in the A35-type systems are not subgiants by evolution, but instead main sequence stars inflated by the recent accretion from the WD progenitor. We base our analysis on the prototypical system, A35, which is the only system with a Gaia astrometric orbit, enabling estimation of the dynamical mass of the components. The rest of the paper is organized as follows. We present our photometric, astrometric and spectroscopic analyses of A35 in Section 2. Here we revise several of the stellar parameters inferred in previous works, and also demonstrate a potential tension between the dynamical and evolutionary mass of the subgiant thus challenging an evolved subgiant scenario). In Section 3 we use state of the art stellar evolution code named Modules for Experiments in Stellar Astrophysics (MESA, Paxton et al. 2011, 2015, 2019) to construct realistic binary evolution models to explain A35-type systems as hosting inflated stars. We also relate these systems to other classes of post-mass transfer systems under a common evolutionary pathway. Finally in Section 4 we present our summary and conclusions.

2. ABELL 35

2.1. Overview and previous works

A35 is a nebula (top panel of Figure 1) which was first discovered by Abell (1955) and was classified as a PN. The central star (henceforth, we simply use A35 to denote the central stellar system rather than the nebula) was first studied in Jacoby (1981) who recognized the binarity of the system and apparently evolved nature of the companion (see Figure 1). The temperature of the subgiant was estimated to be ≈ 5000 K and $\log(g) \approx 3.5$ by photometric comparisons with standard stars. The fast rotation rate of the companion was identified in (Thevenin & Jasniewicz 1997), who estimated a projected surface rotation speed of $v \sin(i) \approx 55$ km s⁻¹. They also reported Ba enhancement in the subgiant. The WD is hot and young with a $T_{\text{eff}} \approx 80$ kK and $\log(g) \approx 7.5$ (Herald & Bianchi 2002; Ziegler et al. 2012, implying a cooling age of $\sim 2 - 5 \times 10^5$ years). The mass of the WD is highly uncertain with estimates (based on comparison with evolutionary models) spanning a broad range of $\approx 0.5 \pm 0.07 M_{\odot}$ across different works (Herald & Bianchi 2002; Ziegler et al. 2012; Löbbling et al. 2020). The separation between the two stars was estimated to be 18 ± 5 AU in (Gatti et al. 1998) using images obtained with the Planetary Camera on Hubble Space Telescope (HST).

¹ This includes WeSb 1, the central star of PN showing signatures of transiting debris disk (Bhattacharjee et al. 2025; Budaj et al. 2025). We introduce WeSb 1 as an A35-type system for the first time in this work, but the details will be presented in a separate letter.

Table 1. Summary of the properties of A35

Parameter	Value
<i>Gaia</i> Properties	
DR3 ID	3499149202247569536
RA (deg)	193.38634
Dec (deg)	-22.87299
Parallax (mas)	6.0339±0.0485
G	9.3583
$G_{BP} - G_{RP}$	1.1510
μ_{α} (mas yr ⁻¹)	-61.611 ± 0.048
μ_{δ} (mas yr ⁻¹)	-13.875 ± 0.019
Radial Velocity	-
Orbital Period (P_{orb})	790.22 ± 2.26 d
Eccentricity (e)	0.0489 ± 0.0064
Inclination (i)	26.09 ± 0.83
Stellar Properties	
Subgiant T_{eff}	4900 ± 50 K
Subgiant radius	3 ± 0.05 R_{\odot}
Subgiant [M/H]	0.00 ± 0.15
Subgiant $v_{rot} \sin(i)$	86 ± 5 km s ⁻¹
Subgiant P_{phot}	0.767 d
WD $T_{eff}^{\#}$	80 ± 10 K
WD $\log(g)^{\#}$	7.2 ± 0.3 K
WD radius	≈(1.7 ± 0.2) × 10 ⁻² R_{\odot}

NOTE—# See Section 2.2.3 for a discrepancy between spectral and photometric properties.

There has been significant uncertainty in the distance to A35, which has often propagated to uncertainty in other parameters. [Jacoby \(1981\)](#) first arrived at a distance of 360 pc by comparing the photometry of the subgiant with template stars. Later, the parallax measured from a Hipparcos single-star astrometric solution ([Perryman et al. 1997](#)) yielded a distance of 163⁺⁹⁶₋₅₈ pc, placing it significantly closer. [Ziegler et al. \(2012\)](#) argued, however, that this distance is incompatible with the inferred WD parameters and preferred the larger subgiant-derived photometric distance.

2.1.1. New results from *Gaia* astrometry

A35 has an astrometric orbital solution from *Gaia* DR3, whose parameters are listed in Table 1. The *Gaia* parallax, corrected for the photo-center motion, is 6.034 ± 0.048 (parallax error has been inflated as per prescription in [Nagarajan](#)

& [El-Badry 2024](#))². This yields a distance of 165.75^{+1.32}_{-1.30} pc, which is consistent with the Hipparcos measurement. The larger photometric distance favored by [Jacoby \(1981\)](#) and [Ziegler et al. \(2012\)](#) is thus ruled out. Throughout the rest of this work, we use the *Gaia* distance for our analysis. The orbit has a period of $P_{orb} = 790 \pm 2$ days and is nearly circular with an eccentricity of $e = 0.049$. Any reasonable estimates of the component masses yields a binary separation of $\lesssim 2$ AU, much closer than estimated in [Gatti et al. 1998](#). The orbital inclination to the line of sight is low at $i = 26.05$ degrees. Samples of the *Gaia* orbit is presented as an inset in the bottom panel of Figure 1 for visualization.

We also discover that A35 is a part of a hierarchical triple system, where the post-mass-transfer inner binary is orbited by a distant tertiary companion identified at a projected separation of 9.56'', corresponding to a physical separation of ≈ 1600 AU at the distance of A35. The tertiary (*Gaia* DR3 3499149202247569408) has a parallax (6.013 ± 0.030 mas) and proper motion ($\mu_{\alpha}, \mu_{\delta} = -60.95 \pm 0.04, -13.39 \pm 0.02$ mas yr⁻¹) that are statistically consistent with those of the inner binary (Table 1), leading to a chance-alignment probability of 8.5×10^{-5} ([Nagarajan & El-Badry 2024](#)). The *Gaia* photometry ($G_{abs} = 8.18$ and $G_{BP} - G_{RP} = 1.94$) and the *gspphot* stellar parameters ($T_{eff} \approx 4126$ K, $\log g \approx 4.66$) indicate a late-type K dwarf with an estimated mass of $\approx 0.65 M_{\odot}$.³ Although the gravitational influence of this tertiary is negligible today, it may have been dynamically important earlier in the system's evolution and played a role in bringing the inner binary to its current configuration (see Appendix A). A detailed study of the role of the tertiary is beyond the scope of this work. But future statistics on the triple fraction of A35-type (or other wide-binary) systems would be informative.

2.2. Stellar Parameters

In this section, we derive constraints on some of the key stellar parameters of A35. A summary can be found in Table 1.

2.2.1. Spectral Energy Distribution

We use the spectral energy distribution (SED) to constrain the temperature of the subgiant, $T_{eff, SG}$, and the radii of both stars (R_{SG} and R_{WD}). We use the synthetic SDSS griz, PanSTARRS y, and Generic/Johnson B and V photometry calculated from the *Gaia* XP spectrum ([Gaia Collaboration et al. 2023](#)), and the *Gaia* G , BP , and RP magnitudes. To incorporate the WD, we use the GALEX NUV and FUV magnitudes, and also the International Ultraviolet Explorer (IUE) HPDP photometry queried from VOSA. We

² Note that the correct parallax is the one provided with the astrometric solution. The single star parallax is higher at 7.30 ± 0.32 and quoted in [Löbbling et al. \(2020\)](#). This is incorrect as A35 has a RUWE of 16 which makes the single star parallax unusable ([El-Badry 2025](#)).

³ estimated using https://www.pas.rochester.edu/~emamajek/EEM_dwarf_UBVIJHK_colors_Teff.txt

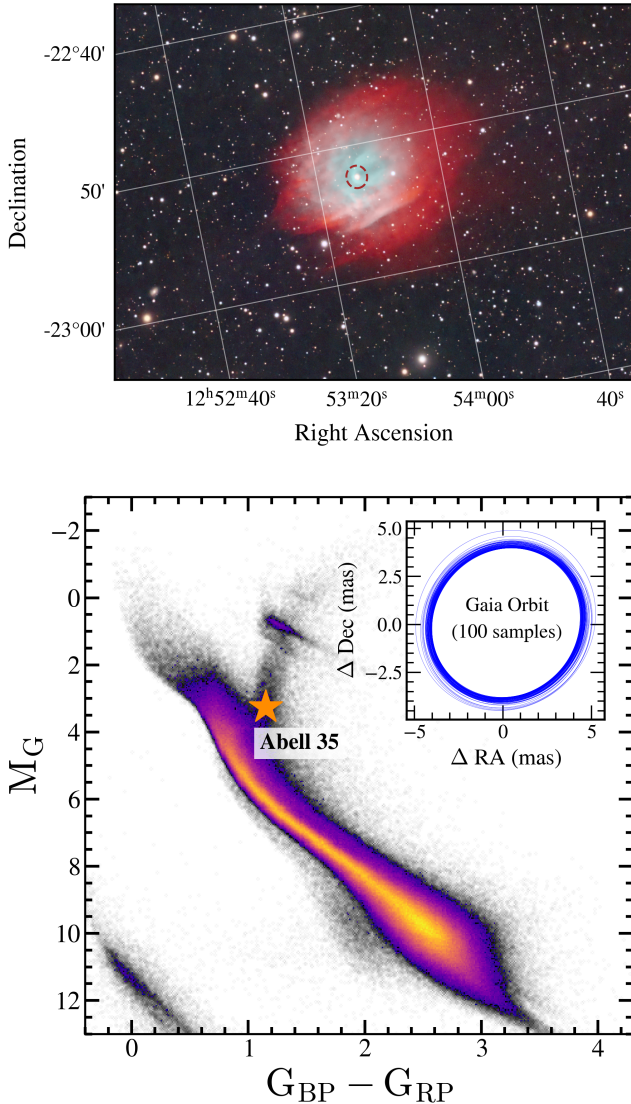


Figure 1. Top panel: The nebula of Abell 35 (A35) with the central (unresolved binary) star marked. Henceforth, we simply call this central star as A35. Bottom panel: The Gaia color-magnitude diagram (CMD) showing the position of Abell 35 (effectively, the companion) in the subgiant branch. The inset presents 100 random samples of the Gaia orbital solution for visualization of the orbit.

adopt an uncertainty floor of 0.03 mag in all bands to account for calibration uncertainties. The source was observed twice by GALEX, yielding significantly different FUV mags of 12.717 ± 0.007 mag and 12.332 ± 0.005 mag. In addition, the GALEX NUV photometry is ≈ 0.1 mag discrepant from the neighboring IUE photometry. This may indicate variability in the UV; we conservatively inflate the GALEX uncertainties to 0.2 mag. We use the PHOENIX stellar models (Husser et al. 2013) for the subgiant and TMAP models

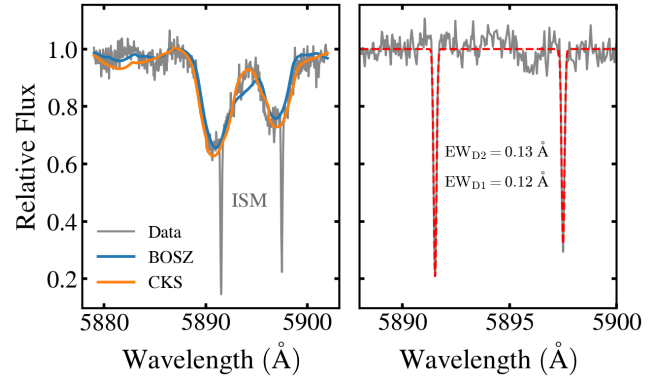


Figure 2. Inferring the reddening from the high resolution optical spectrum of the subgiant obtained with FEROS. Left panel: Normalized stellar spectrum around the Na-D doublet. The narrow ISM lines are well resolved. We overplot a (suitably rotationally broadened) synthetic spectrum from BOSZ and a stellar spectrum from the CKS survey best matching the observed Na-D lines in A35. The details about the spectral analysis are presented in Section 2.2.2. Right panel: Spectra further normalized by the best-matching templates. Gaussian profile fits to the ISM lines and the corresponding equivalent widths (EWs) are shown.

(Rauch & Deetjen 2003)⁴ for the WD to generate synthetic spectrum. We then use the `pyphot` package to calculate the magnitudes at the respective photometric bands. Finally, to perform the fit, we use `emcee` implementation of MCMC (Foreman-Mackey et al. 2013) with simple χ^2 loss function.

For the subgiant, the two free parameters are $T_{\text{eff, SG}}$ and R_{SG} . We keep the surface gravity fixed at $\log(g) = 3.5$. This is motivated from the previous studies (and consistent with our final inferences). Additionally, the SED is not significantly sensitive to this parameter. We keep the metallicity fixed. We primarily use a solar metallicity but also explore other values within the uncertainties derived in Section 2.2.2. For the WD, we rely on the parameter and abundance estimates in Herald & Bianchi (2002); Ziegler et al. (2012): $T_{\text{WD}} = 80 \pm 10$ kK, $\log(g) = 7.5$ and $X(\text{He}) = 0.4$ and obtain the appropriate TMAP models. We use each model separately. Thus, the only free parameter for the WD is R_{WD} . We use broad uniform priors for all our parameters. We keep the distance fixed at the Gaia distance of 165.75 pc.

The uncertain parameter that significantly affects our results is the reddening. Herald & Bianchi (2002) estimated $E(b-v) = 0.04 \pm 0.01$ using the Rayleigh-Jeans tail of the WD, whereas Ziegler et al. (2012) suggests a lower range of $E(b-v) = 0.02 \pm 0.02$. The reddening estimated from three-dimensional dust maps at the distance of A35, however, are

⁴ Downloaded from TMAP webpage: http://astro.uni-tuebingen.de/~rauch/TMAF/flux_H+He.html

much higher: $E(b-v) \approx 0.09$ as per Green et al. (2019)⁵ and ≈ 0.06 as per Wang et al. 2025⁶.

We perform a fresh estimate of the reddening from the equivalent width (EW) of the interstellar Na-D doublet lines, resolved in our high resolution optical spectroscopic observations (presented in Section 2.2.2). We obtain a combined equivalent width of $EW_{\text{Na D1+D2}} = 0.26 \text{ \AA}$ (see Figure 2). Following the prescription in Poznanski et al. (2012), this yields a reddening of $E(b-v) \approx 0.03 \pm 0.005$. Note that this is broadly consistent with the estimates from the WD spectra and photometry in (Herald & Bianchi 2002; Ziegler et al. 2012), but significantly lower than those inferred from the dust maps. The reason behind such a discrepancy is unclear.

We perform the SED fit two ways. First, we keep $E(b-v)$ ⁷ as a free parameter. The fit converges at $E(b-v) = 0.047 \pm 0.023$ and yields a subgiant temperature of $T_{\text{eff, SG}} = 4956 \pm 58 \text{ K}$, radius of $R_{\text{SG}} = 2.93 \pm 0.03$ and a WD radius (with $T_{\text{eff, WD}} = 80 \text{ kK}$) of $R_{\text{WD}} = (1.7 \pm 0.2) \times 10^{-2} R_{\odot}$. Manual inspection, however, shows that a $E(b-v) > 0.04$ underestimates the WD flux in the far-UV when compared to the archival spectrum from the Far Ultraviolet Spectroscopic Explorer (FUSE). Thus, next, we fix $E(b-v)$ to the Na doublet-derived reddening of 0.03. This yields a slightly lower subgiant temperature of $T_{\text{eff, SG}} = 4914 \pm 19 \text{ K}$, the same R_{SG} , but a smaller WD radius of $R_{\text{WD}} = (1.62 \pm 0.02) \times 10^{-2} R_{\odot}$. There is no appreciable change in the results with changing the metallicity within the limits discussed in Section 2.2.2. Thus, overall, we provide the final range of subgiant parameters as: $T_{\text{eff}} = 4925 \pm 75 \text{ K}$ and $R_{\text{SG}} = 2.95 \pm 0.05 R_{\odot}$. Within the T_{WD} range of Ziegler et al. (2012), we find the WD radius to lie in the range of $R_{\text{WD}} \approx (1.75 \pm 0.25) \times 10^{-2} R_{\odot}$.

2.2.2. Spectroscopic analysis of the Subgiant

We observed A35 with Fiber-fed Extended Range Optical Spectrograph (FEROS; Kaufer et al. 1999) instrument installed on the MPG/ESO 2.2m telescope at the La Silla Observatory (program 115.28KE.001). We obtained six observations of 600 seconds exposure between April and August, 2025. We used 1×1 binning. This allowed us to achieve a spectral resolution $R \sim 50,000$ over 3860 \AA to 6770 \AA . For a single observation, the median signal-to-noise ratio (SNR) achieved was ≈ 60 . We reduced the raw data using the CERES pipeline (Brahm et al. 2017).

Prior to performing any analysis, we pseudo-continuum normalize the spectra as follows. First, we clip $C = 20 \text{ \AA}$ from both ends of each spectral order, where the noise becomes large. We then smooth the spectrum using a $W_s = 1 \text{ \AA}$ box kernel to remove noise. Following this, use a moving box

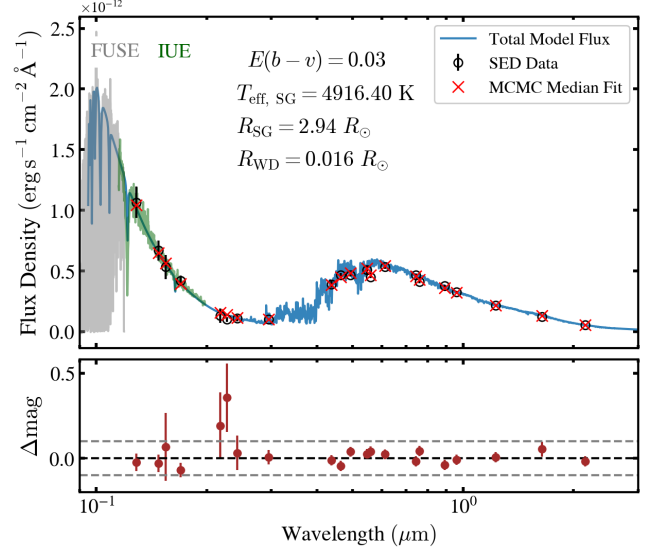


Figure 3. The SED of A35 (black circles) and our best fit PHOENIX+TMAP model with a fixed $E(b-v)=0.03$ (blue line). This fit uses a solar metallicity for the subgiant and a temperature of 80 kK for the WD. The corresponding synthetic photometry from our model is shown as red crosses. We also present the FUSE (grey) and IUE (green) spectra. The PHOENIX spectrum is downresolved for clarity. The bottom panel shows the deviation of the best-fit synthetic magnitudes from those observed. The horizontal lines denote ± 0.1 mag derivation. The single discrepant point is GALEX NUV.

of width $W_n = 10 \text{ \AA}$ and determine the $N = 10^{\text{th}}$ largest data point of the smoothed data within the window. We then linearly interpolate on these points to define the pseudo-continuum. The choice of the aforementioned parameters of this routine is arbitrary. But our results are not significantly sensitive to details in the continuum normalization, since we normalize models and data using the same procedure. We merge orders into a single spectrum, co-adding individual orders in overlap regions.

We do not detect any radial velocity (RV) variation in our spectrum. At the Gaia orbital period and inclination, any reasonable assumption of the binary component masses yields a RV semi-amplitude of a few kilometers per second. However, owing to the heavy rotational blending of the absorption lines, potentially augmented by surface magnetic wind/spot activity, our RV uncertainties are larger than this.⁸ Thus, to improve SNR, we co-add all the six spectra. But we verify that our inferences do not change if the single epoch spectra are used instead.

The two primary properties we aim to constrain are the metallicity, $[\text{Fe}/\text{H}]$, and the projected surface rotational speed, $v_{\text{rot}} \sin(i)$ of the subgiant. Accurately determining

⁵ Queried using the online tool at <http://argonaut.skymaps.info/>

⁶ Queried using the Python package `dustmaps3d`.

⁷ All dust extinction corrections were performed using the `dust_extinction` (Gordon 2024a,b) implementation of the Gordon et al. (2023) galactic extinction models (Declair et al. 2022; Gordon et al. 2021; Fitzpatrick et al. 2019; Gordon et al. 2009).

⁸ We see a scatter of $\approx 5 - 10 \text{ km s}^{-1}$ in the measured RVs, depending on the models and spectral region used. But this is not a systematic error of the spectra as the ISM Na-D lines do not show this shift. Thus we attribute it to the overall RV uncertainty.

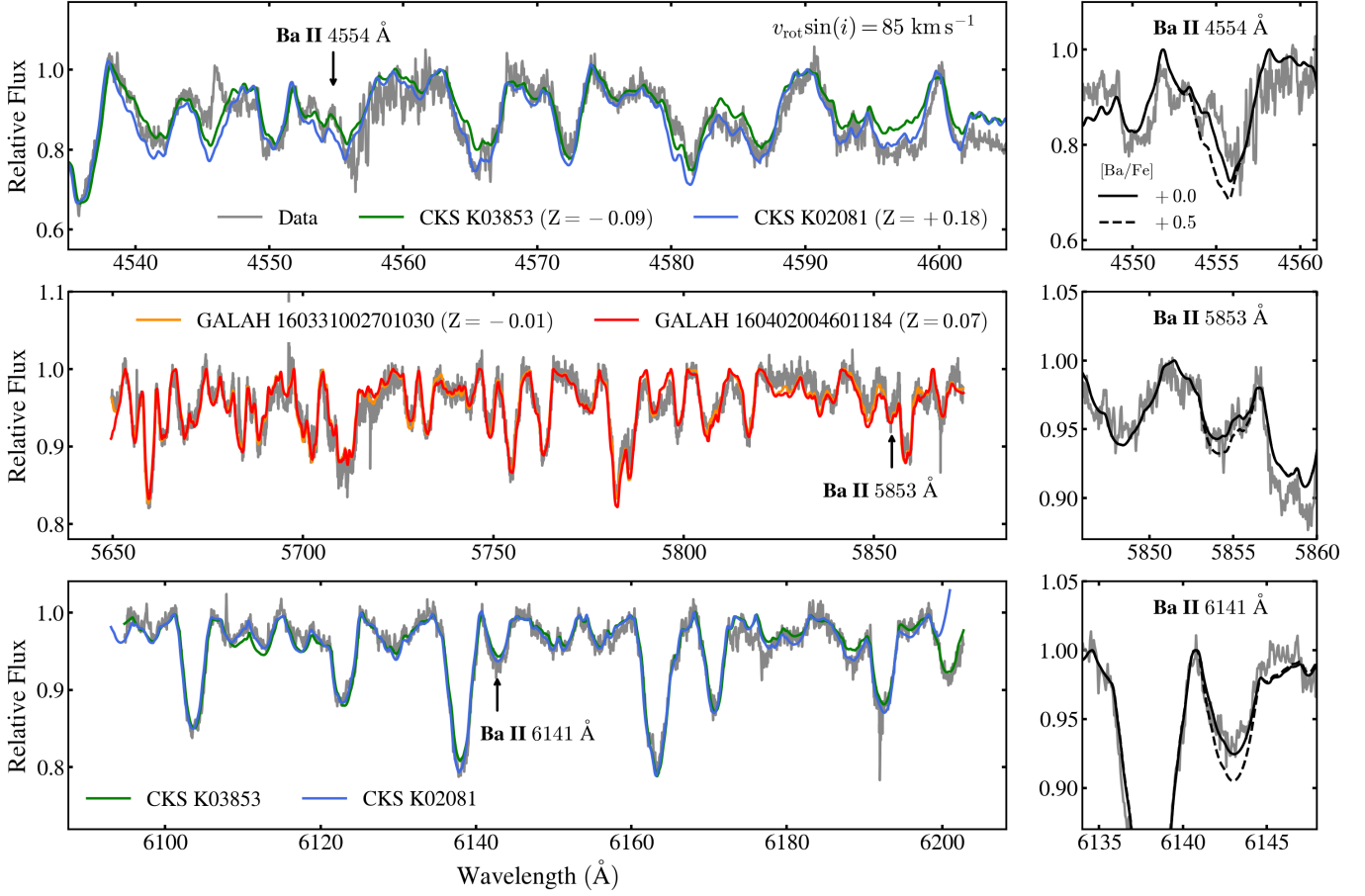


Figure 4. Left three panels: Comparison of the FEROS spectrum of the subgiant in A35 with GALAH and CKS spectra for three wavelength ranges, each containing a strong Ba II line. The good match indicates a new-solar metallicity of the subgiant and no significant Ba excess. Right panel: Zoom-in on the Ba lines and comparison with synthetic spectra of $[M/H] = -0.1$ from *iSpec*, with and without Ba excess. The latter yields a much better match indicating no significant Ba enhancement.

$[\text{Fe}/\text{H}]$, in this case, is challenging due to the heavy rotational blending of the absorption lines, augmented by the uncertainties with spectral models. We thus experimented with several different approaches, which we discuss below. A combined estimate of the two parameters are listed in Table 1.

Comparison with BOSZ models—First, we used the BOSZ synthetic spectral library (Bohlin et al. 2017; Mészáros et al. 2024). We use templates with $R = 50,000$, which is well-matched to the FEROS data. Based on the temperature constraint from the SED, we retrieved all spectra with $T_{\text{eff}} = 4750$ K and 5000 K and $\log(g) = 3.5$ from the publicly available database⁹, and normalized them using the same routine described above. To avoid un-physical degeneracies, we restrict a few model parameters to values reasonably expected for a subgiant like A35. Specifically, we only consider models with alpha-element abundance of $[A/M] \leq +0.25$, carbon abundance of $[C/M] = +0.0$, and microturbulent velocity of $v_{\text{micro}} \leq 2$ km s⁻¹. This yields a total of 126

templates. To incorporate the sensitivity of our results to the wavelength range being considered, we employ a heuristic method of dividing the FEROS spectrum into consecutive segments of 50 Å. For each segment, we iterate through all the templates, finding the corresponding best-fit $v_{\text{rot}} \sin(i)$ and RV over a suitable grid and record the χ^2 .¹⁰ We estimate the best-fit parameters for each segment as the mean parameters of the 20 templates with the lowest χ^2 . Finally, we combine the estimates from all the segments by computing the mean and standard deviation.

Overall, we obtain a net metallicity estimate of $[M/H] \approx -0.04 \pm 0.2$. This is broadly consistent with that estimated in Thevenin & Jasniewicz (1997) ($[\text{Fe}/\text{H}] \approx -0.2 \pm 0.3$), and that estimated in Andrae et al. (2023) from Gaia XP

¹⁰ To estimate the wavelength-dependent error in the calculation of χ^2 , we first smooth the data using a Savitzky-Golay filter followed by computing the local standard deviation of the residuals from the smoothed data.

⁹ <https://archive.stsci.edu/hlsp/bosz>

spectrum ($[M/H] = -0.14 \pm 0.15$)¹¹. A mild alpha enrichment of $[A/M] \approx +0.05 \pm 0.2$, along with a microturbulent velocity of $\approx 1.3 \pm 0.8 \text{ km s}^{-1}$ are favored. We obtain a mean temperature of $\approx 4917 \pm 118 \text{ K}$, consistent with our inference from the SED.

We obtain a more precise estimate of the projected rotational velocity of $v_{\text{rot}} \sin(i) = 86 \pm 5 \text{ km s}^{-1}$. This is significantly higher than estimated in (Thevenin & Jasniewicz 1997, $\approx 55 \text{ km s}^{-1}$). We now relate our revised estimate to the photometric period of 0.767 days (noted in Jacoby 1981, and also recovered in the most recent TESS light curve¹², see Bond & Zeimann 2024). Assuming this to be the rotational period, the estimated radius of the subgiant gives an equatorial rotational velocity of $v_{\text{rot}} = 2\pi R_{\text{SG}}/P_{\text{rot}} \approx 195 \pm 3 \text{ km s}^{-1}$. This implies an inclination of the rotation axis of $i \approx 26.2 \pm 1.7$ degrees. This is in perfect agreement with the Gaia orbital inclination, and indicates an alignment of the rotational and orbital axes, as expected for accretion-induced spin-up.

Comparison with SPECTRUM models—Next, we use another set of synthetic spectral models generated using the radiative transfer code SPECTRUM¹³ Gray & Corbally (1994). We use the python interface provided by `iSpec` (Blanco-Cuaresma et al. 2014; Blanco-Cuaresma 2019). We generate a grid of models varying T_{eff} between 4700 K and 5400 K at an interval of 50 K, $[M/H]$ between -0.5 and $+0.5$ at an interval of 0.05, and $[\alpha/\text{Fe}]$ between 0.0 and 0.2 at an interval of 0.1. We keep surface gravity fixed at $\log(g) = 3.5$. This yields a total of 900 model spectra. `iSpec` generates normalized models, which we re-normalize using our custom method to maintain consistency with the data. We perform a similar analysis with the BOSZ models, where we chose the top 20 best-fit models for a given segment and take the mean and standard deviation of the associated parameters.

Overall, we obtain similar results across different spectral regions, with the best-fit metallicity value lying in the range of $[M/H] \approx -0.05 \pm 0.15$. This is consistent with the BOSZ estimate. These models, however, favor slightly lower temperatures, broadly in the range of $4850 \pm 75 \text{ K}$, still consistent with the previous estimates. We find $[\alpha/\text{Fe}]$ to mostly take values $\lesssim 0.1$. The $v \sin(i)$ estimate remains consistent at $\approx 86 \pm 2 \text{ km s}^{-1}$.

Comparison with GALAH spectra—Spectral models do not perfectly reproduce observed spectra. Thus, we resort to another more empirical approach of comparing A35 spectra with other stellar spectra from high-resolution spectral libraries. We first use the GALAH DR4 HERMES spectral library (Sheinis et al. 2015; Buder et al. 2025). We use all spectra with $4700 \text{ K} \leq T_{\text{eff}} \leq 5100 \text{ K}$, $3.25 \text{ K} \leq \log(g) \leq 3.7$

and $\text{SNR} \geq 75$. This yields a total of 584 spectra. The spectra are available over four channels (B , V , R , and I) spanning four different wavelength ranges. We use only the first three, as the fourth covers a wavelength range beyond our FEROS data. We again perform a χ^2 minimization selection individually for the three channels. The third GALAH channel contains $\text{H}\alpha$, where A35 shows emission due to chromospheric activity and/or nebular contamination. We masked $\approx 30 \text{ \AA}$ on either side of $\text{H}\alpha$ before calculating χ^2 .

This empirical exercise favors higher metallicity values in the range of $[\text{Fe}/\text{H}] \approx 0.12 \pm 0.10$, still broadly consistent with the previous estimates at close to solar metallicity. The $v \sin(i)$ estimate from GALAH is consistent with the previous estimates of $85 \pm 3 \text{ km s}^{-1}$. The $T_{\text{eff SG}}$ and $\log(g)$ estimates take values of $4950 \pm 60 \text{ K}$ and 3.4 ± 0.1 , consistent with all previous estimates. A comparison of the A35 spectrum with two of the best-fit GALAH spectra in V -channel is shown in Figure 4.

Comparison with CKS spectra—To assess the robustness of our estimates, we use the Keck/HIRES spectra from the California-Kepler Survey (CKS, Petigura et al. 2017; Johnson et al. 2017), primarily to investigate the range of wavelengths not covered by the GALAH HERMES spectra. Because the CKS library is much smaller than GALAH, we only compare the FEROS spectrum of A35 to the CKS spectra of stars with parameters closest to the best-fit values from the GALAH comparison. We show the results in the first and third panels of Figure 4 for two CKS spectra of $[\text{Fe}/\text{H}] = +0.17 \text{ dex}$ and $[\text{Fe}/\text{H}] = -0.1 \text{ dex}$ ¹⁴. We find that the higher metallicity spectrum appears to fit some of the strong Fe line regions better, for example the line complexes around 4566 \AA (first panel in the figure) and 6137 \AA (last panel), which speaks against the lower metallicity inference from BOSZ (or previous studies). Overall, combining BOSZ, GALAH and CKS comparisons, we conclude that A35 is likely to be close to solar metallicity.

Lack of significant Ba enhancement—Unlike Thevenin & Jasniewicz (1997), we do not find evidence for significant Ba enhancement. In the left three panels of Figure 4 we mark three strong Ba lines at 4554 \AA , 5853 \AA , and 6141 \AA . We find the GALAH/CKS spectra, none with any significant Ba excess, match the strength of the observed Ba lines quite well. We further investigate this by generating synthetic spectra using `iSpec` with varying Ba abundance. For this, we set $T_{\text{eff}} = 4900 \text{ K}$, $\log(g) = 3.4$, and conservative $[M/H] = -0.1$. We present a zoom-in on the Ba lines in the right panels of the same figure, where we compare the A35 data with two `iSpec` spectra with $[\text{Ba}/\text{Fe}] = 0.0 \text{ dex}$ and $[\text{Ba}/\text{Fe}] = +0.5 \text{ dex}$. We find that the former fits the data significantly better than the latter. We note, however, that within the noise level of the FEROS spectrum, the Ba abundance cannot be obtained at a precision better than ≈ 0.3

¹¹ This value has been obtained from R. Andrae over private communication, involving a revised calculation using the Gaia NSS parallax instead of the single star parallax used in the original work.

¹² <https://www.tessextractor.app/>

¹³ <https://www.appstate.edu/grayro/spectrum/spectrum.html>

¹⁴ these are metallicity values estimated using spectra and isochrones jointly, Johnson et al. 2017 provided in `iso_met` column in the CKS catalog

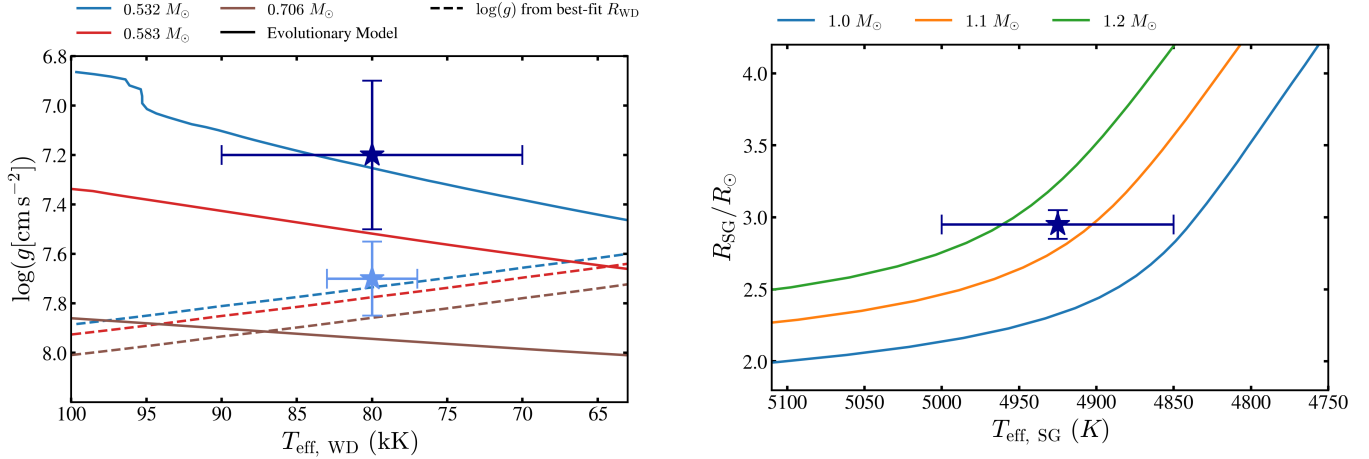


Figure 5. Left panel: The spectroscopic $\log(g)$ and T_{eff} of the WD from Ziegler et al. (2012, dark blue star) and Herald & Bianchi (2002, light blue star) compared to the post-AGB tracks from (Miller Bertolami 2016, solid lines) for $Z = 0.01$ (model file 0100.t03.dat.txt). We also plot the $\log(g)$ derived from the radii that best fit the IUE photometry as discussed in Section 2.2.3 (dashed lines). Intersection of the solid and dashed lines within the error ellipse of A35 would signify a consistent solution. No consistent solution exists for the Ziegler et al. (2012) parameters. A potential solution exists for $M_{\text{WD}} \approx 0.6 M_{\odot}$ with the parameter estimates from Herald & Bianchi (2002). Right panel: The photometric parameters of the subgiant compared to the MIST models of solar metallicity, yielding a best evolutionary mass estimate of $1.1 \pm 0.1 M_{\odot}$. Uncertainty in metallicity results in an additional uncertainty of $\approx 0.1 M_{\odot}$.

dex. Thus any enhancement below this limit cannot be confidently ruled out.

2.2.3. Mass of the WD

The hot WD, BD−22°3467, was first systematically studied in (Herald & Bianchi 2002) using spectral data from IUE, HST, and FUSE. They arrived at a $T_{\text{eff}} = 80 \pm 3$ kK and $\log(g) \approx 7.7 \pm 0.15$. They reported a very broad range of WD mass of $0.5_{-0.4}^{+0.5} M_{\odot}$. Later, Ziegler et al. (2012) re-analyzed the data and revised the $\log(g)$ to a lower value of 7.2 ± 0.3 . Comparing to the post-EHB tracks of Dorman et al. (1993) and post-AGB tracks of Miller Bertolami (2016), they estimated a WD mass of $0.48 \pm 0.05 M_{\odot}$. However, the mass estimate was later revised in Löbbling et al. (2020) to a higher value of $0.533_{-0.025}^{+0.04} M_{\odot}$.

In the two latest studies, the distance to the source was assumed to be ≈ 360 pc. This yields a WD radius of $\approx 0.03 R_{\odot}$, making it consistent with evolutionary parameters discussed in those works. However, as shown in Section 2.2.1, the revised Gaia distance yields a much smaller radius. This leads to tension between the spectroscopic parameters and post-AGB evolutionary models. We demonstrate this in the left panel of Figure 5. We plot the post-AGB tracks from Miller Bertolami (2016) and the error margins of A35 from Ziegler et al. (2012, dark blue). To incorporate the constraints from the SED, we perform the following exercise. We take the T_{eff} values provided by the model and calculate a white dwarf radius that best-fits the IUE photometry. From the WD mass, we then calculate a predicted $\log(g)$ ¹⁵. We call this the photo-

metric $\log(g)$ and plot it in the same figure. We see that there is no consistent solution to the spectroscopic and photometric $\log(g)$ within the error margin provided in Ziegler et al. (2012). However, if we allow higher values of $\log(g) \gtrsim 7.6$, a consistent solution is found at $M_{\text{WD}} \gtrsim 0.57 M_{\odot}$ and $T_{\text{eff}} \lesssim 75$ kK. In fact, a higher $\log(g)$ is consistent with the inferences of Herald & Bianchi (2002, shown in the same figure in light blue), though their error in T_{eff} maybe underestimated. In fact, a consistent solution exists within the Herald & Bianchi (2002) parameter range for $M_{\text{WD}} \approx 0.62 M_{\odot}$.

The imperfect agreement between photometric, spectroscopic, and evolutionary parameters may imply that the uncertainties on the spectroscopic parameters are underestimated. It might also be a result of binary interaction leaving the WD with a thicker hydrogen shell than would be found for a single WD of the same mass.

2.3. Disfavoring an evolved subgiant: A post-mass transfer inflated star instead?

As briefly discussed in Section 1, the subgiant nature of the companion is intriguing. The key to distinguishing between a true evolved star from an inflated star is to look for discrepancy between the subgiant mass and the mass of the WD progenitor. This is because, given the young age of the WD, the former scenario requires a near-equal initial masses of the two components (twin binary; mass ratio $\lesssim 1.015$ in our case). We first attempt to estimate the subgiant mass by comparing the SED-derived subgiant parameters to MIST (Dotter 2016; Choi et al. 2016) evolutionary models, with the evolved scenario being the null hypothesis. Within the metallicity uncertainty, this leads to a range of possible subgiant masses of $0.9 M_{\odot} \lesssim M_{\text{SG}}^{\text{MIST}} \lesssim 1.3 M_{\odot}$. Assuming typical initial to final mass ratios (IFMR, Cunningham et al. 2024), the

¹⁵ The TMAP models are available at a T_{eff} interval of 10 kK. For intermediate temperatures, we performed a linear interpolation over models by keeping $\log(g) = 7.5$ fixed.

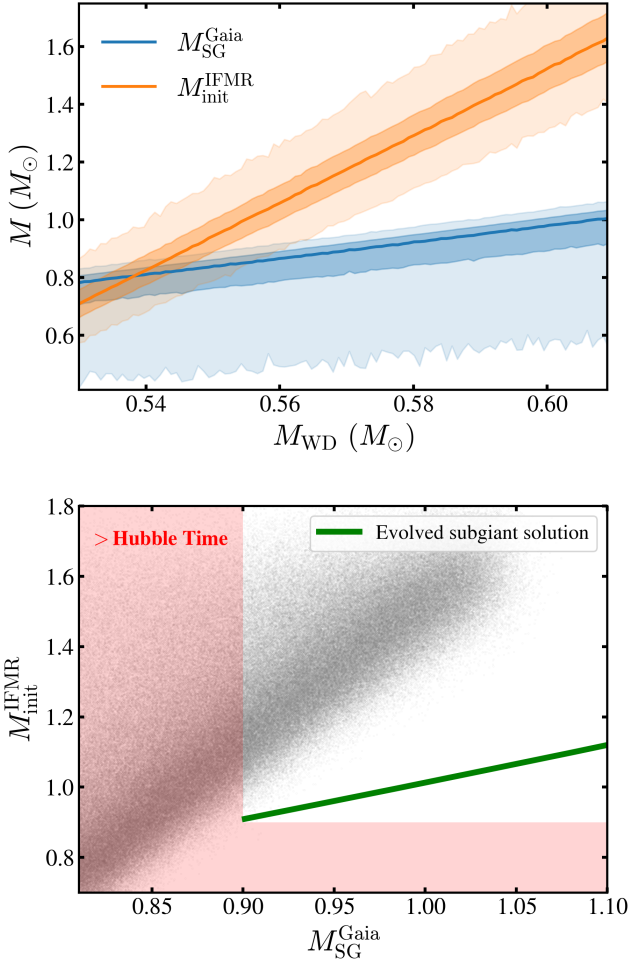


Figure 6. Examining the evolved subgiant scenario. Top Panel: Subgiant mass permitted by Gaia astrometry (M_{SG}^{Gaia} , blue) and the initial mass of the WD (M_{init}^{IFMR} , orange), estimated using the IFMR from [Cunningham et al. \(2024\)](#), as a function of the assumed WD mass. The dark (light) shaded region represents (1σ) 3σ -equivalent error region on either side of the median values (solid line). The intersection of the shaded regions is the twin-binary solution space. Bottom Panel: All the M_{SG}^{Gaia} and M_{init}^{IFMR} pairs from our uniform Monte Carlo sampling of WD masses. The region where either of the masses is $<0.9 M_{\odot}$ is shaded in red and excluded. The green line shows the MIST-estimated masses for which the companion can evolve to its present (subgiant) radius. A twin-binary solution would require the two components to fall on this line and thus is strongly disfavored.

WD’s initial masses also fall in the this, thus appearing consistent. However, the uncertainties are too broad to detect any finer discrepancy.

The Gaia astrometric solution, however, provides an additional constraint for the component masses. But, without any reliable RV information, the individual masses cannot be inferred uniquely. We thus perform the following exercise. We draw WD masses uniformly between $0.53 M_{\odot}$ and

$0.61 M_{\odot}$. For each WD mass, we obtain the posterior of the Gaia astrometry-allowed subgiant masses. We do this by randomly drawing the Gaia orbital parameters within their respective error regions and solving the Keplerian orbital equation (see Appendix B). We employ appropriate correction for the WD flux contribution to the Gaia photocenter, with a G-band flux ratio of $F_{G, WD}/F_{G, SG} = 0.9\%$. We then convert the assumed WD masses to an initial mass using the IFMR derived in [Cunningham et al. \(2024\)](#). This IFMR is not directly calibrated for initial masses $<1 M_{\odot}$. We perform a simple extrapolation of Equation 1 in their paper, which is adequate for our purpose. Finally, we compare the IFMR-derived initial masses with the astrometry-allowed subgiant masses. Given an initial mass, we use MIST models to estimate the mass of the companion which can evolve to its present (subgiant) radius at the appropriate age.

The result is shown in Figure 6. Firstly, very low subgiant mass of $\lesssim 0.9 M_{\odot}$ can be ruled out since the main-sequence lifetime of such stars at the metallicity of A35 exceeds the Hubble time. For higher masses, it is evident that a twin binary solution is unlikely as the astrometry-allowed WD mass is much higher than can be produced by a star of the subgiant’s mass. This discrepancy is further augmented by two additional reasons:

- The IFMR used is for single stars. The binary interaction between the WD progenitor and the companion, however, has the potential to substantially truncate the mass of the resultant WD when compared to single stars of similar masses. This is witnessed in several recent works where the binary IFMR is seen to significantly deviate from that of single stars, especially for the lower end of WD masses (see, for example, [Ironi et al. 2025](#); [Shahaf 2025](#)). A truncation of the WD mass (i.e. higher M_{init}^{IFMR} for a given M_{WD}) will further disfavor a twin binary scenario.
- Assuming a fiducial $M_{SG} \approx 0.95 M_{\odot}$ yields a surface breakup speed of the star of $v_{break} \approx 250 \text{ km s}^{-1}$. This makes the measured $v_{rot} \approx 80\%$ of the break-up speed. This makes it reasonable to assume that, during mass transfer, the star was spun up to almost its break-up speed (post which it has spun-down to its present value). Assuming a Keplerian angular momentum of the accretion disk, the accretion mass needed to achieve the observed v_{rot} is given by:

$$M_{acc} = \left(\frac{I_{SG}}{M_{SG} R_{SG}^2} \right) \frac{v_{rot}}{v_{break}} M_{SG}, \quad (1)$$

which, in this case, yields $M_{acc} \approx 0.06 M_{\odot}$ (assuming a fiducial sun-like radius of gyration). This needs to be subtracted from the current mass estimates to get the true initial mass of the subgiant. This would make the discrepancy with a twin-binary solution more pronounced.

Finally, as already discussed in Section 1, a twin binary origin of the whole population of A35-type systems is unlikely. This presumably extends to this object as well.

This shows that it is very unlikely for the subgiant to be a naturally evolved star. Rather, the hypothesis of it being a main-sequence star which is inflated from a recent mass transfer episode (Neo et al. 1977a; Fujimoto & Iben 1989; Lau et al. 2024; Zhao et al. 2024) is favored. In the next section, we investigate this hypothesis further by exploring realistic binary evolution models with MESA.

3. ACCRETOR RESPONSE IN MESA BINARIES

Several past works studying the response of the accretor have used single-star models accreting at a constant rate (Kippenhahn & Meyer-Hofmeister 1977; Neo et al. 1977a; Fujimoto & Iben 1989; Zhao et al. 2024; Lau et al. 2024). Though this has provided invaluable insights on the accretor response, a primary limitation of such an approach is its inconsistency with binary evolution models, which usually predict the mass transfer rate to vary by several orders of magnitude during the mass-transfer process. Such an approach also cannot self-consistently predict whether the mass transfer will proceed stably or the accretor will fill its own Roche lobe and trigger CEE.

Here, we extend the previous works to full MESA binary simulations, evolving both the stars self-consistently through mass transfer. In our calculations, the accretor indeed inflates substantially, but remains within its Roche lobe, allowing the mass transfer to proceed stably. Post-mass transfer, the inflated accretor gradually relaxes back toward main sequence. We conjecture that the A35-type systems lie in this relaxation phase and present an opportunity to test models for accretor inflation. Additionally, we find that our models can potentially unify several post-mass transfer populations under the same evolutionary pathway.

3.1. Method

We use the latest MESA version of `r24.03.1`. We use the `MESABinary` module and set `evolve_both_stars=.true.` We use the accretion prescription by Kolb & Ritter (1990). For the component inputs, we use a solar metallicity of $Z = 0.014$ for both the stars. We use the Ledoux (1947) criterion to determine convective instability, use a mixing length Cox & Giuli (1968) parameter of $\alpha = 1.9$, and also include semiconvection with $\alpha_{sc} = 0.1$ (Choi et al. 2016; Temmink et al. 2023). We also model winds following Choi et al. (2016) and Temmink et al. (2023): Reimers (1975) wind for RGB phase with a scaling factor of $\eta_R = 0.1$ and Bloeker (1995) wind for AGB phase with $\eta_B = 0.2$. Additionally, we assume non-conservative mass transfer, with only 50% of the transferred mass being accreted (i.e., $\beta = 0.5$; Soberman et al. 1997; the rest being lost from the vicinity of the accretor).¹⁶ We also include con-

vective overshoot, similar to Yamaguchi et al. (2024b) and Lau et al. (2024). We use a step overshoot scheme for the core, with $f/f_0 = 0.129/0.0129$ and exponential scheme for the shell with $f/f_0=0.0174/0.00174$. We use `energy_eqn_option = 'dedt'`.

By default, we set `gold_tolerances` to `.false.` Our models run successfully through the mass transfer phases with `gold_tolerances` turned on. But we do not show them because, for unclear reasons, they crash during the early WD cooling sequence and, thus, do not span enough for our figures that follow. We also tested that increasing the spatial/temporal resolutions do not affect the results significantly apart from increasing the run-time. For our fiducial A35 model (model A, described in Section 3.2.1), we use here the output from a simulation with increased accretor spatial resolution of `mesh_delta_coeff=0.25` which yields results very similar to `gold2_tolerance=.true.` but does not terminate prematurely.

3.1.1. New Accretion Prescription

The default accretion prescription of MESA is to set the thermodynamic properties of the accreted material (namely, the pressure, energy, and density) to those of the stellar photosphere. The rationale behind this treatment might be that most of the gravitational potential energy of the in-falling material gets radiated or dissipated away in the accretion disk, resulting in a smooth deposition of mass on the stellar surface. But this argument has certain limitations, as the accreted material may have much higher temperature and entropy than the stellar surface, because of the gravitational energy liberated during its in-fall. Whether it is shock-heated via direct impact accretion, or viscously heated in an accretion disk or boundary layer, the accreted material is expected to deposit a significant amount of excess energy/entropy.

On a different note, we also find that with the fiducial prescription, MESA fails to converge at high accretion rates of $M \gtrsim 10^{-3} M_{\odot}/\text{yr}$, especially for low accretor masses of $\lesssim 1 M_{\odot}$. The reason is unclear, but it is likely of numerical origin and may be related to the steep entropy gradients at the surfaces of stars with convective envelopes.

We thus modify the thermodynamic properties of the accreted material via a custom accretion prescription in MESA. We do this by setting `use_other_accreting_state=.true.` in the `inlist` for the accretor. We then use `run_star_extras.f90` to set the new prescription. We assume that the matter falls from infinity with no initial kinetic energy and is virialized upon reaching the stellar surface. We assume that only a fraction f_E of the initial potential energy is retained and deposited onto the stellar surface. Considering a Keplerian accretion disk yields $f_E = 0.5$.

¹⁶ Note that MESA defines β as the fraction of the mass lost instead, so the `inlists` should be read accordingly.

This yields the following prescription:

$$\begin{aligned} v_a &= \sqrt{\frac{2f_E GM_*}{R_*}}; \\ E_a &= (f_E - 1) \frac{v_a^2}{2f_E}; \\ \rho_a &= \frac{\dot{M}}{4\pi R_*^2 v_a}; \\ P_a &= \rho_a v_a^2, \end{aligned} \quad (2)$$

where v_a , E_a , ρ_a , and P_a denote the radial velocity, total specific accretion energy, density, and pressure of the in-falling material, respectively. We assign E_a , ρ_a , and P_a to the function arguments `total_specific_energy`, `accretion_density`, and `accretion_pressure`, respectively. For all our models we use $f_E = 0.5$, but find that other values yield qualitatively similar results.¹⁷ Note that, in this new prescription, the density of the in-falling material is a function of \dot{M} , which is physically expected, unlike in the default MESA prescription which further justifies its revision.

3.1.2. Estimating the accretor spin

As discussed earlier, the accretor is expected to spin up almost to its breakup speed potentially after accreting only a small fraction of its mass (Packet 1981). The default settings of MESA are to enhance mass loss when the spin approaches breakup to prevent further accretion. However, several studies suggest that this may not be the correct picture, and the star can keep accreting matter (without gaining angular momentum, Popham & Narayan 1991). Additionally, a model with rotation is more prone to numerical instabilities. Thus, we do not include rotation in our models. Instead, we calculate the stellar angular velocity, Ω , as a post-processing step from the model outputs. Specifically, we employ a finite difference method using MESA's timesteps to compute Ω using the following evolution equation:

$$\dot{\Omega} = \frac{\dot{J}_{\text{acc}} + \dot{J}_{\text{MB}} - I_* \dot{\Omega}}{I_*}. \quad (3)$$

Here, I_* is the moment of the inertia of the accretor which we consistently calculate inside our models as $I_* = \frac{2}{3} \int R^2 dm$. \dot{J}_{acc} is the angular momentum gained through accretion, for which we assume the angular momentum of a Keplerian orbit at the stellar surface:

$$\dot{J}_{\text{acc}} = \dot{M} \sqrt{GM_* R_*}. \quad (4)$$

\dot{J}_{MB} is the angular momentum lost through magnetic braking, for which we use the prescription from Rappaport et al.

(1983):

$$\dot{J}_{\text{MB}} = -0.5 \times 10^{28} \left(\frac{I_*}{M_* R_*^2} \right) R_\odot^4 \left(\frac{R_*}{R_\odot} \right)^\gamma \omega^3, \quad (5)$$

and use $\gamma = 4$ (Rappaport et al. 1983; Gossage et al. 2023). If at any timestep $\Omega > \Omega_{\text{crit}}$, we force $\Omega = \Omega_{\text{crit}}$. We recognize that this step may have non-trivial implications for a thermally contracting star. Conserving angular momentum, $\Omega \sim R^{-2}$ (assuming a roughly constant I/MR^2), whereas $\Omega_{\text{crit}} \sim R^{-1.5}$. Thus, $\Omega/\Omega_{\text{crit}} \sim R^{-0.5}$. Therefore, during contraction without any angular momentum loss, the rotation rate with respect to critical should, in fact, increase. However, by forcing $\Omega/\Omega_{\text{crit}} = 1$, we are artificially draining angular momentum. In reality, this may be driven by centrifugally enhanced mass loss from the star during this phase. Overall, we emphasize that this rotation rate calculation maybe far from reality. But Equation 3 nevertheless provides a simple method to predict the star's rotation evolution that can be calibrated and compared to observations.

3.2. Results

3.2.1. Model overview

We now present some models that approximately reproduce the observed properties of A35 and its class. We have not carried out an exhaustive search of the parameter space to best-match the system's properties but only endeavor to identify the typical evolutionary histories that can give rise to A35-type systems. We find that several initial configurations can reasonably produce A35-type systems, thus relaxing the need for any fine-tuning to explain this population. Overall, our models start with an unequal-mass binary ($q \sim 0.5$), where the more massive star ($M > 1.0 M_\odot$ for A35) evolves off the main sequence and transfers mass to its less massive companion ($M < 1 M_\odot$) with an initial period of $\sim 10^3$ days. Depending on the exact parameters, the mass transfer can occur when the donor is on the RGB, forming a low-mass ($M_{\text{WD}} \lesssim 0.48 M_\odot$) WD, or when it is on the AGB, forming a more massive ($M_{\text{WD}} \gtrsim 0.53 M_\odot$) WD. The accretor gains a significant amount of mass, and expands in radius substantially, briefly reaching up to $\sim 10^2 R_\odot$, simultaneously spinning up to critical rotation. It then contracts towards the main sequence, passing through an A35-like state around $\sim 10^5$ years after mass transfer ends, when it is still inflated and rotating fast.

We will discuss three representative models (models A, B, and C) with different initial parameters. All the three models have an initial donor mass of $M_d = 1.2 M_\odot$. Models A and C have an initial companion (i.e. accretor) mass of $M_a = 0.5 M_\odot$ and $\beta = 0.5$ but differ in their initial period of $P_i = 1000$ days and 600 days, respectively. For Model B, we use a much lower $\beta = 0.05$ with a period similar to Model A. For fair comparison, we make $M_{a, B} = 0.7 M_\odot$ so that the final mass of the accretor becomes comparable to the other two models.

We first discuss the overall response of the accretor and the change in its properties over the course of binary evolution and mass transfer. In Figure 7, we present the trajectory

¹⁷ Inspection shows that not all values of f_E are numerically stable, especially when $f_E \lesssim 0.2$. Thus, we keep the study of the quantitative dependence of our results on f_E for a future more detailed work on accretion models.

Table 2. The other A35-type systems. For A35¹, refer Table 1.

Name	Gaia DR3 ID	RUWE	Distance (pc)	$T_{\text{eff, SG}}$ (K)	R_{SG} (R_{\odot})	$T_{\text{eff, WD}}$ (kK)	R_{WD} ($0.01 R_{\odot}$)	P_{orb} (d)	e	$E(b-v)$	P_{phot} (d)	$v_{\text{rot}} \sin(i)$ (km s^{-1})
LoTr 1 ⁶	2917223705359238016	1.49	$1791.3^{+53.9}_{-47.7}$	4590	9.7	$\gtrsim 120$	≈ 1.7			0.07	6.4	
WeSb 1 ^{7,9}	423384961080344960	1.10	$3334.0^{+254.5}_{-310.2}$	6500	6.0					0.6		90
LoTr 5 ^{11,12,13}	3958428334589607552	2.19	$449.7^{+8.9}_{-9.1}$	5100	10			≈ 2700	0.25	0.0	5.9	66
WeBo 1	465640807845756160	1.44	$1499.9^{+41.1}_{-49.5}$	4720	7.5					0.6	4.7	
Pa 27 ²	1859955657931121536	1.07	$1436.6^{+22.7}_{-23.9}$	4760	8.55					0.28	7.6	
Hen 2-39 ¹⁴	5256396485463285504	1.03	$8814.5^{+1929.3}_{-1614.2}$	4350	14					≈ 0.5	5.4	38^{+5}_{-5}
Abell 70 ⁸	6907822573352460032	1.03	$3628.5^{+1459.4}_{-1010.8}$	≈ 5000	> 1.5	$\gtrsim 120$		$\gtrsim 720$	$\gtrsim 0.3?$	0.07	2.07	37^{+5}_{-5}
UCAC2 ¹⁰	1391041780057897856	2.51	$1200.9^{+39.4}_{-30.9}$	4790	5.2	105^{+5}_{-5}	$4^{+0.5}_{-0.4}$			0.0	1.99	81

References—1) This work, 2) Bond & Zeimann (2024), 3) Herald & Bianchi (2002), 4) Ziegler et al. (2012), 5) Löbbling et al. (2020), 6) Tyndall et al. (2013), 7) Bhattacharjee et al. (2025), 8) Jones et al. (2022), 9) Bhattacharjee et al. in prep. 10) Werner et al. (2020), 11) Jones et al. (2017), 12) Aller et al. (2018), 13) Van Winckel et al. (2014), 14) Löbbling et al. (2019)

NOTE—Except for Hen 2-39, where the distance is uncertain, we re-performed the SED fit, following the same method as Section 2.2.1, to obtain the subgiant parameters consistently. All of our values are broadly in agreement to those previously reported in literature.

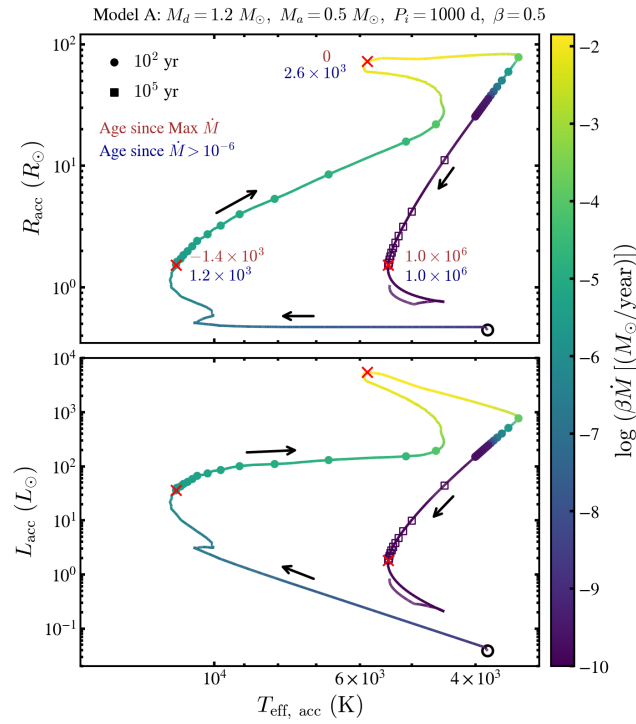


Figure 7. Top Panel: Evolution of radius (R_{acc}) and temperature ($T_{\text{eff, acc}}$) of the accretor in model A over the course of the binary evolution, colored according to $\beta \dot{M}$. The black open circle marks the beginning of the model, and the arrows mark the direction of evolution. The filled circles (open squares) mark the intervals of 10^2 (10^5) years – only for the regime where $R_{\text{SG}} > 1.5 R_{\odot}$ to focus on the inflated state of the accretor. We also provide the ages, since beginning of mass transfer and since the maximum \dot{M} , at three representative epochs marked with red crosses. Bottom Panel: Evolution shown in the Hertzsprung-Russel diagram. Overall we find that the accretor rapidly inflates in $\sim 10^4$ years and then begins to contract once mass transfer ends. The contraction slows as the star approaches the main sequence over $\sim 10^6$ years.

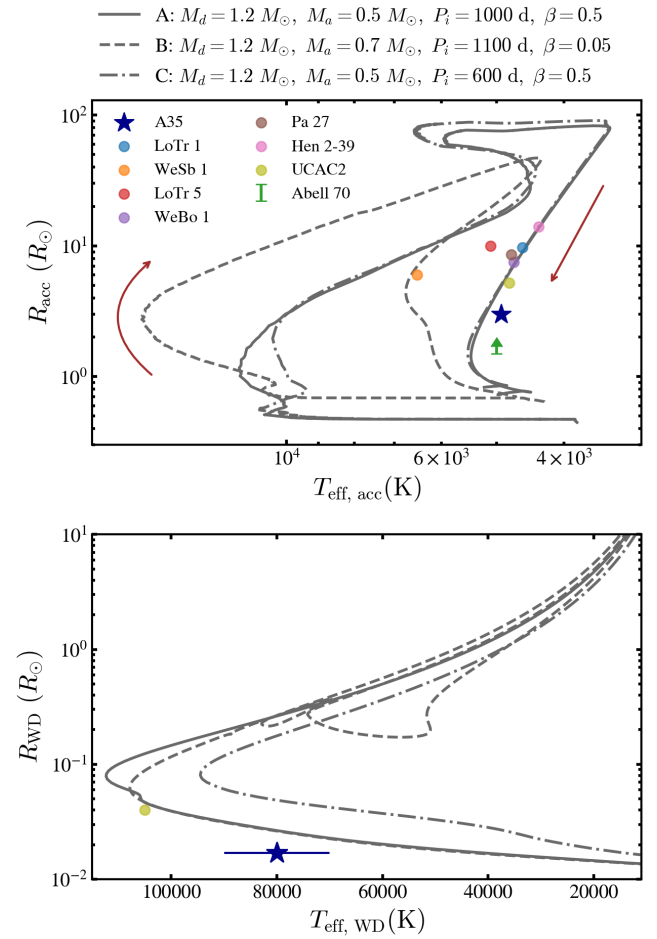


Figure 8. Top panel: Evolution of the accretor in $R-T_{\text{eff}}$ space. We show three models with the same initial donor mass, but different accretor mass, initial orbital period, and β (see label on top). We plot the stellar parameters of the subgiants in all known A35-type systems for comparison. Bottom panel: Evolution of the donor. We plot the WD parameters of A35 and UCAC2. We find the models to broadly reproduce the diversity of the observed population.

of the accretor in $R_{\text{SG}} - T_{\text{eff, SG}}$ space. For ease of discussion, we only present Model A, but the behavior is qualitatively similar for the other models (Figure 8). At the initial period of this model, appreciable mass transfer happens only during the AGB phase of the donor (Model C is different in this aspect as there the mass transfer occurs during RGB, forming a low mass WD), and driven by the thermal pulses. When the accretor appreciably fills the Roche lobe, \dot{M} rises steadily. We find that, across all scenarios, the accretor first becomes significantly hotter very quickly at the onset of accretion. This is followed by a rapid expansion and cooling over a timescale of $\sim 10^3$ years. In this model, it reaches a peak radius of $\approx 80 R_{\odot}$. The accretion rate attains very high values of $\sim 10^{-2} M_{\odot}/\text{year}$ but only for a very brief period of ≈ 20 years. Soon after, \dot{M} drops rapidly as the donor loses most of its envelope, leaving behind an inflated and spun-up accretor and a rapidly contracting donor.

3.2.2. Comparison with A35-type systems

The inflated accretor contracts over its thermal timescale, relaxing back to the main sequence, but still remaining appreciably inflated for around a million years. We propose that A35-type systems represent this phase of contraction where the accretor is still inflated and rotating fast. To show this, we compare the subgiant parameters of the known A35-type systems (see Table 2) to the MESA models. This is presented in the top panel of Figure 8. We clarify here that our models shown here are tailored for A35, and it is not expected that these will directly explain all the other systems. Nevertheless, we find that most of the systems lie close to our MESA model tracks. In the bottom panel, we also present the post-AGB evolution of the donor. Only two A35-type systems have spectroscopically derived WD parameters. We show them for comparison.

Focusing on A35, we find that model A comes closest to explaining this system (both stellar and binary parameters), though we include the other two models for demonstrating the effects of the key model parameters. We note though, that none of our models can exactly meet the A35 parameters on all fronts. For example, in all our ‘best-fit’ models, the subgiant temperature is $\approx 250 \pm 50$ K higher than that of A35 at its radius. Such a discrepancy can arise from the following effects: 1) the spots on the stellar surface can bias its observed temperature to lower values, 2) the centrifugal force from the rotation and/or the magnetic pressure can compensate for thermal pressure, resulting in its lower temperature. Given the complexity of the inflation process and significant uncertainties in several parameters and physics, we consider such differences acceptable.

3.2.3. Mass transfer stability at high \dot{M}

A key uncertainty in our models stems from the very high mass transfer rates of $\gtrsim 10^{-2} M_{\odot}/\text{year}$ that they reach during mass transfer that begins high on the RGB or AGB. Though the models do not fail to converge or experience accretor Roche lobe overflow, the evolution becomes uncertain

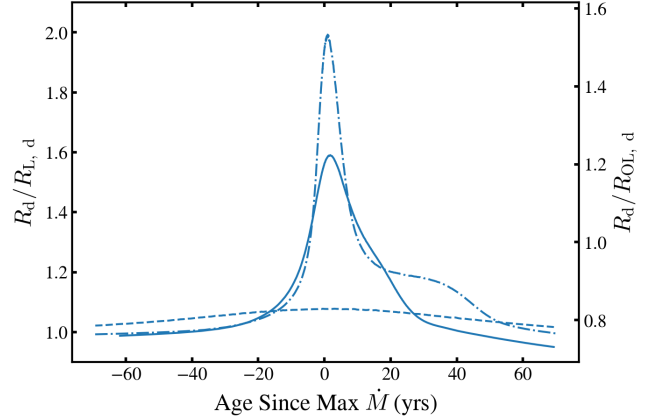


Figure 9. Roche Lobe ($R_{L,d}$) and Outer lobe ($R_{OL,d}$) overfill factors of the donor around the epoch of the highest accretion rates. For all our models, $R_{OL,d}/R_{L,d} \approx 1.3$ during this epoch (calculated using equation 4 in Temmink et al. 2023). Thus, we have used this single scaling value for the right axis. We follow the same linestyles for the models as in Figure 8.

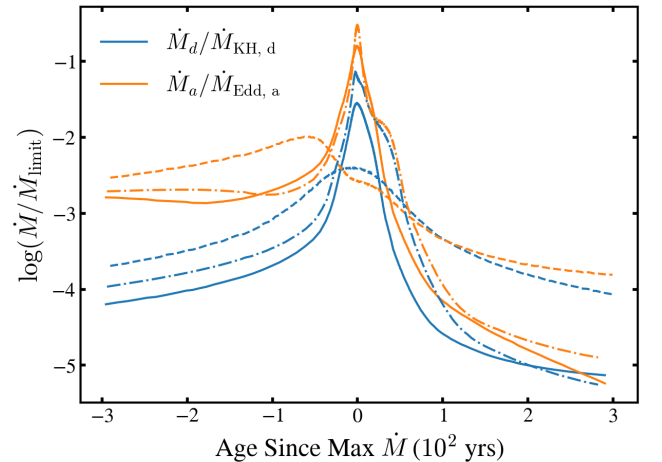


Figure 10. Ratio of the 1) donor mass loss rate rate, $\dot{M}_d \approx \dot{M}$, to the global thermal timescale of the donor $\dot{M}_{\text{KH},d}$ (blue lines) and 2) accretor’s accretion rate $\dot{M}_a \approx \beta \dot{M}$ to the Eddington-limited accretion rate $\dot{M}_{\text{Edd},a}$. We only show ± 300 years around the epoch of peak mass transfer. Both the limits are always satisfied, indicating plausible stability. We follow the same linestyles for the models as in Figure 8.

at such high \dot{M} values, potentially making them vulnerable to instability and CE. At the epochs of highest \dot{M} , the donor in models A and C achieve un-physically high values of Roche lobe overfill factors (albeit for a very brief period of a few tens of years, Figure 9, top panel) where the conventional mass transfer prescriptions break down. Additionally, the donor also overfills its outer (L3) lobe (same figure, only mildly for model A but substantially for model C). The associated mass loss from L3 can drain angular momentum, thus bringing the stars closer and triggering CEE.

However, the study by [Temmink et al. \(2023\)](#) suggests that neither of the above necessarily trigger an instability. Thus, we perform a few additional tests. We compare \dot{M} to the accretion rate limited by the global thermal timescale of the donor (equation 6 in [Temmink et al. 2023](#)):

$$\dot{M}_{\text{KH, d}} = 6.7 \times 10^{-7} \left(\frac{M_d}{M_\odot} \right)^{-1} \frac{R_d}{R_\odot} \frac{L_d}{L_\odot} M_\odot/\text{year}. \quad (6)$$

The mass transfer is likely to remain stable when $\dot{M} < \dot{M}_{\text{KH}}$ ([Ge et al. 2020](#)). Note that this is a stricter stability criterion than the quasi-adiabatic criterion derived in [Temmink et al. \(2023\)](#). Additionally, we compare $\beta\dot{M}$ (the effective accretion rate) to the Eddington rate of the accretor (equation 9 in [Neo et al. 1977b](#)):

$$\dot{M}_{\text{Edd, a}} = 1.24 \times 10^{-3} \frac{R_a}{R_\odot} M_\odot/\text{year}. \quad (7)$$

We present this comparison in [Figure 10](#) for all the three models. We find that our mass transfer rates are always contained within the two limits, showing that stability can possibly be maintained even at such accretion rates. This is in line with several recent works showing that mass transfer from RGB/AGB stars may frequently remain stable ([Ge et al. 2020](#); [Temmink et al. 2023](#); [Yamaguchi et al. 2025](#)). Our models also show that although accretors expand significantly in response to mass transfer, they may often not fill their Roche lobes in AU-scale orbits. Nevertheless, there may be additional factors driving instability which we discuss in [Section 3.5](#). We note here that in Model B, though \dot{M} attains similarly high values, $\beta\dot{M}$ remains below $10^{-3} M_\odot/\text{year}$. The accretor thus gains very little mass. Nevertheless, it still inflates significantly showing that the accretor can inflate even without accreting a large amount of mass.

3.2.4. Time Evolution

We now discuss how the stellar and binary properties evolve with time after mass transfer stops. We show this in [Figure 11](#). We concentrate on the periods after maximum \dot{M} . We find that the accretion rate decreases to $\sim 10^{-5} M_\odot/\text{yr}$ within 100 yr, and to $\sim 10^{-10} M_\odot/\text{yr}$ within 10^4 yr. By this time, both the stars have settled at their final masses. In Models A and C, the accretor gains a substantial amount of mass of $0.25 M_\odot$ and $0.35 M_\odot$, respectively. In Model B, due to low β , only a few $\times 10^{-2} M_\odot$ is gained. The binary period has also attained its final value of $\sim 10^3$ days. During this time, the inflated accretor is relaxing back to the main sequence and the donor is rapidly contracting and heating up, forming a WD. We find that a post-mass transfer age range of $10^4 - 10^6$ years best correspond to the observed properties of A35-type systems (shaded in green in the figure). After a few million years, the accretor has relaxed back to the main sequence and the WD has entered the cooling track.

It is worth discussing the evolution of the rotational speed of the accretor separately. As mentioned earlier, the accretor attains a critical rotation rate soon after the accretion of a

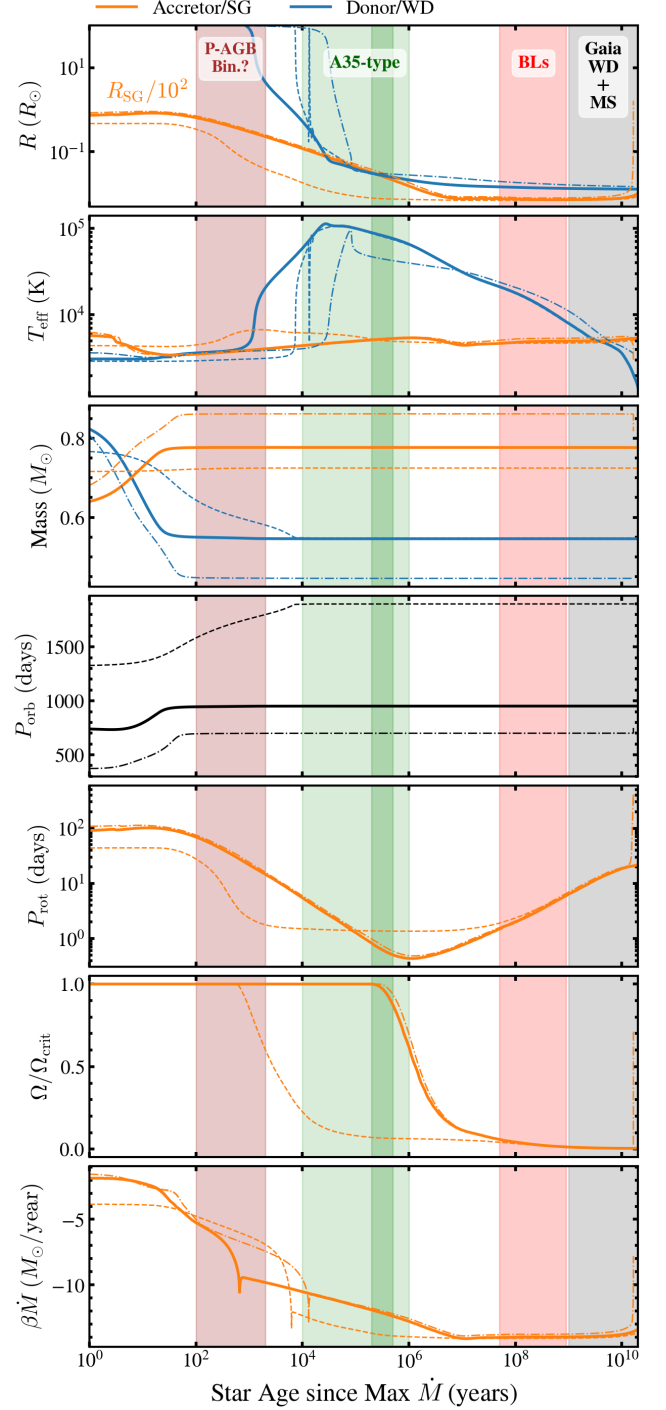


Figure 11. Evolution of stellar and binary parameters after maximum \dot{M} for all three models (highlighting Model A for clarity). We denote the accretor and donor with blue and orange colors, respectively. The age range approximately satisfying the properties of the A35-type systems is shaded in green, with darker shading corresponding to A35 in particular. The age range for Post-AGB Binaries (P-AGB Bin.), Blue Lurkers (BLs) and Gaia WD+MS population are shaded in brown, red and gray, respectively. We follow the same linestyles for the models as in [Figure 8](#).

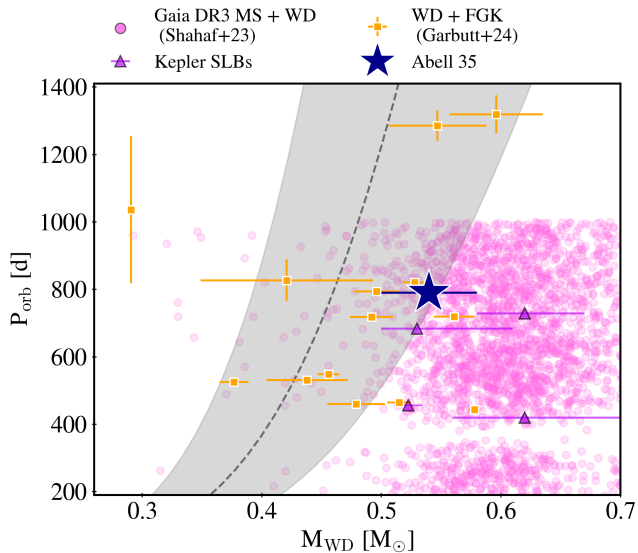


Figure 12. Orbital periods and WD masses for A35 and several other classes of related post-mass transfer binaries. The Rappaport et al. (1995) relation for stable RGB mass transfer is shown as dashed line and a shaded error region. A35 seems most similar to the Gaia WD+MS binaries and the Kepler SLBs, which are both plausibly the results of AGB mass transfer.

small fraction of its mass, and remains critically rotating until the end of interaction. Critical rotation is also maintained during the initial contraction phase till the star has contracted to a radius $\lesssim 10 R_{\odot}$. This is because, though the critical angular velocity (Ω_{crit}) increases as the star contracts, the rotation rate also increases to conserve angular momentum. This also leads to a decrease in P_{rot} . Within the age range of A35-type systems, our models yield $P_{\text{rot}} \sim 1 - 10$ days, in good agreement with observations. At late times, magnetic braking takes over, draining angular momentum and increasing P_{rot} to $\mathcal{O}(10 \text{ d})$ over the next 10^9 years.

3.3. Evolutionary connection to other populations

We now discuss the evolutionary link between A35-type binaries and other post-mass transfer binaries. Figure 12 shows A35 in the parameter space of the orbital period, P_{orb} , and the WD mass, M_{WD} . In the same figure, we plot the analytic $P_{\text{orb}} - M_{\text{WD}}$ relation for post-stable mass transfer on the RGB derived in Rappaport et al. (1995). We also show several other classes of post-mass transfer systems namely the Gaia WD+main sequence population (Yamaguchi et al. 2024b; Shahaf et al. 2023), the Kepler SLBs Kruse & Agol (2014); Kawahara et al. (2018); Masuda et al. (2019); Yamaguchi et al. (2024a), and the UV-excess WD+FGK binaries (Garbutt et al. 2024). It is evident that A35 occupies the same position in the parameter space as the other systems. Owing

to the lack of reliable masses¹⁸ for most Blue Lurkers (BLs, WDs with fast rotating main sequence companions, Leiner et al. 2019; Nine et al. 2023), we do not include them in the plot. Future spectroscopic surveys will populate this plot further.

Our MESA models naturally establish a connection between these different populations. We again refer to Figure 11. As already discussed, A35-type systems constitute the regime where the accretor is thermally relaxing back to main sequence and has just started to spin-down through magnetic braking. Following the models forward, we find that $\text{few} \times 10^8$ years later, the white dwarf has cooled to temperatures $\lesssim 30 \text{ kK}$ and the accretor has relaxed back to the main sequence. However, it is still rotating rapidly with $P_{\text{rot}} \lesssim 10$ days. We propose that these constitute the BLs (shaded in red in the figure). Further into the future at several billion years post-mass transfer, the WD has cooled further and the accretor has spun-down significantly. At this stage, the accretors' bulk properties are indistinguishable from those of normal MS stars. This stage constitutes the bulk of wide WD+main sequence stars (primarily from Gaia, shaded in gray in the figure). We depict this evolutionary pathway pictorially in Figure 13. We emphasize that this discussion should be interpreted with caution as the specifics of the formation history of each individual system may differ (like the BL WOCs 14020, where the donor is proposed to be a merger product, Leiner et al. 2025). The unifying scheme, however, is the accretion-induced inflation and subsequent evolution of both the WD and the accretor.

Another related population, which can be viewed as the progenitor population for A35-type binaries, is the post-AGB (or RGB, but we use this term universally for our purpose) binaries (van Winckel 2003). These comprise of a rapidly contracting post-AGB star with a companion (mostly of unknown nature) at orbital periods similar to the other populations (Oomen et al. 2018). As the donor has not yet become a WD, these are systems even younger than A35-types with a post-mass transfer age of less than a few thousand years (shaded in brown in Figure 11). Our models imply that the accretor should be significantly inflated at this stage. The system may thus appear as composed of two evolved stars. In fact, a few such systems are already known, namely HD 172481 (Reyniers & Van Winckel 2001) and SS Lep (Verhoelst et al. 2007). We conjecture that one of the two stars in these binaries is an inflated star. Interestingly, Jorissen et al. (2009), in their Section 2.2, discusses the possibility that several of the stars cataloged as post-AGB can very well be inflated accretors. Our models support this possibility.

Most of the companions to post-AGB stars are thought to be main sequence stars (Oomen et al. 2018). But most

¹⁸ Except for WOCs 14020, but the WD here is proposed to be from a merger product in an initially triple system (Leiner et al. 2025). Photometric estimates are available for a few BLs, for those maybe unreliable (note, for example, the significant revision of the mass estimate for WOCs 14020 in Nine et al. 2023 vs Leiner et al. 2025).

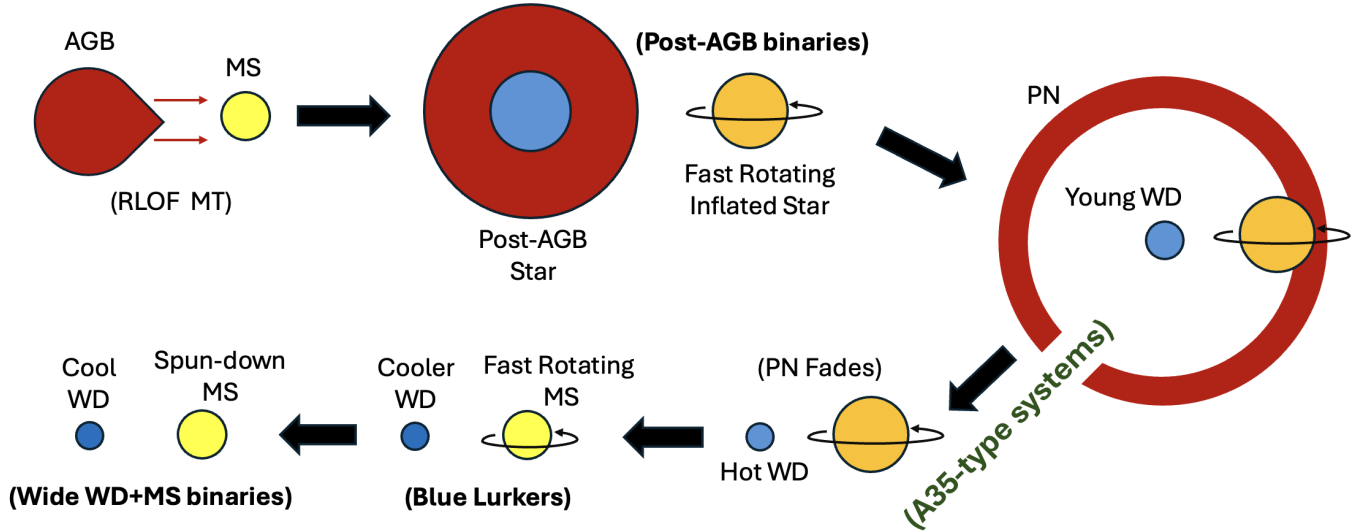


Figure 13. Cartoon depicting the proposed evolutionary sequence connecting the different observed populations of post-mass transfer wide binaries.

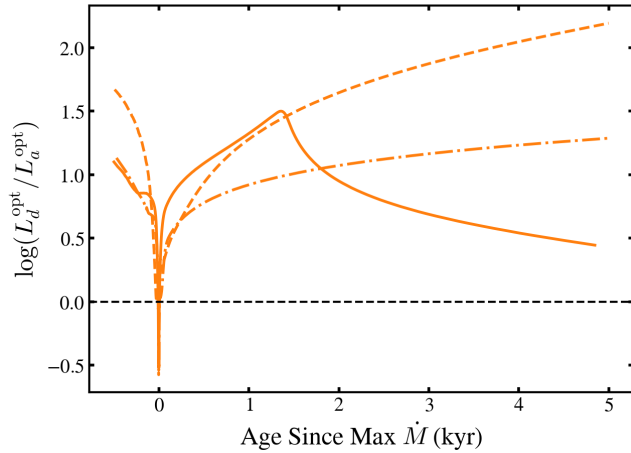


Figure 14. Ratio of the donor to accretor luminosity in the optical (0.5 – 0.7 nm, assuming blackbodies) in the approximate age range of the post-AGB binary systems. In all our models, despite the accretor’s inflation, the donor dominates the optical light after peak mass transfer. We follow the same linestyles for the models as in Figure 8.

studies arrive at this conclusion by ruling out a WD companion, which does not necessarily rule out giant or sub-giant companions. For example, [Hillen et al. \(2016\)](#) presents IRAS 08544-4431 as the only post-AGB system where the flux from the companion is detected in the infrared, where they note the possibility of the companion being a red-giant. The other reasoning behind the assumption of a main sequence companion can be the lack of significant flux contribution from the companion in the SED/optical spectra. But, this is not surprising as, despite being inflated, the accretor can be sub-luminous. This is also what we find in our models – the donor dominates the optical (and bluer) wavelengths till at least $\sim 10^4$ years post mass transfer (Figure 14). The com-

panion can possibly be detected in the infrared (as in [Hillen et al. 2016](#)), which, unfortunately, is often dominated by the dust emission.

3.4. Observational Predictions

We now present some predictions which can motivate future observations and test our models:

- As the PN timescales are shorter than stellar inflation timescales, there should be more A35-type systems outside PNe. Till now, the search for these systems have mostly been focused inside PNe, significantly limiting the scope of identifying these systems. A broader search for such systems is being undertaken through spectroscopic follow-up of subgiant stars with UV excess, the results of which will be presented elsewhere ([Bhattacharjee et al. in prep.](#)).
- In all our models, the accretor relaxes back to the main sequence within a few million years of the accretion episode. This time-span is relatively short compared to the WD cooling timescale. Thus, the prediction is that most AU-scale companions to hot (i.e., $T_{\text{eff, WD}} \gtrsim 50$ kK) should appear evolved. In the other way, most AU-scale WD companions to main sequence stars should be ‘cool’. These are presently in line with 1) with the known WD temperatures in BLs, and 2) lack of any known main sequence companions to hot WDs. This maybe partly influenced by detection bias towards bright giant companions. But given that most of the A35-type systems should have also been detected if the companions were main sequence stars, a significant bias seems unlikely. Nevertheless, more extensive UV spectroscopic follow-up of WD+main sequence binaries ([Yamaguchi et al. in prep.](#)) and dedicated searches for companions to hot WDs should be performed.

- The companions to most post-AGB binaries should appear evolved. Our discussion in the previous section shows that such a possibility cannot yet be ruled out with the current data. Future observations dedicated to the detection and study of the companion are needed.

3.5. Caveats

The primary caveat of our models is the uncertainty in the evolution during the highest accretion rates of $\dot{M} \gtrsim 10^{-2} M_{\odot}/\text{year}$. Recent works, for example by Lu et al. (2023); Scherbak et al. (2025), have shown that there can be mass loss from L2 at such high accretion rates. Though this is most likely to happen when the accretion rate surpasses the Eddington limit – not the case with our models – we do not rule an L2 outflow. Also, the donors in our model often fill the outer lobe (Figure 9), which lead to L3 mass loss. Both these would have the same effect of draining a significant amount of angular momentum, shrinking the orbit and likely triggering CE. In MESA, L2 mass loss can in principle be mimicked using the δ mass loss parameter, which drains angular momentum through a circumbinary disk. But we do not attempt this as such models tend to be highly unstable and uncertain. Additionally, owing to the large Roche lobe overflow factors in our models (Figure 9), the epochs of highest \dot{M} , including the maximum inflated radius, should be interpreted with caution. However, the evolution of the accretor post-mass transfer is expected to be sufficiently reliable that our proposed evolutionary picture is not affected by these limitations.

A second caveat concerns the effects of rotation and magnetic fields, which we have not self-consistently modeled in the MESA calculations. Both of these can provide additional pressure support, which can assist in the inflation of the star. A spin-up may also enhance stellar winds which can drain angular momentum in a more complicated way than assumed in the magnetic braking law incorporated in our calculations. Additionally, a 1D evolution code like MESA is not enough to capture all the complicated physics. In the future, detailed 3D simulations of interacting binaries may shine further light on how stars respond to rapid accretion

4. SUMMARY AND CONCLUSIONS

Abell 35 (A35) type systems are peculiar binaries comprised of a very hot and young WD (with effective temperatures of $\sim 10^5$ K) and a fast-rotating subgiant companion in a ‘wide’ ($\sim 10^3$ day period) orbit. There are eight known systems, six of which are young enough to be inside planetary nebulae. The fast rotation of the subgiant hints at a recent accretion episode, presumably from the WD progenitor giant star. In this work we revisit this population of systems, primarily to shed light on their formation channel and establish their significance in the broader context of post-mass transfer evolution. Specifically, we argue that the subgiants in these systems are likely to be main sequence stars temporarily inflated through the recent accretion episode. We anchor our analysis to the prototype system A35 – the only system to have an astrometric binary solution in Gaia DR3.

Firstly, the Gaia parallax yields a distance of 165.75 pc, significantly closer than assumed in Jacoby (1981) and Ziegler et al. (2012). The system has an orbital period of 790 d, comparable to other populations of au-scale WD+MS binaries recently identified with Gaia. In light of this astrometric orbit and aided by new spectroscopy of the subgiant companion, we construct MESA binary evolution models to study the inflation of the accretor. Below, we present our inferences in further detail.

Our primary inferences from the joint analysis of Gaia astrometry, SED and high-resolution spectrum of A35 are as follows:

1. The subgiant parameters: A fit of the spectral energy distribution (SED) yields a temperature of 4925 ± 75 K and a radius of $2.95 \pm 0.05 R_{\odot}$ (Figure 3). Analysis of the FEROS spectrum yields a high surface rotation speed of $v \sin(i) = 86 \pm 5$ km s $^{-1}$, which corresponds to a surface rotation speed of $v_{\text{rot}} \approx 196$ km s $^{-1}$. This is near the critical rotation velocity and substantially higher than found in normal subgiants. Comparing the optical spectrum of the subgiant in A35 with synthetic templates and stellar libraries, we arrive at a metallicity of $[\text{Fe}/\text{H}] \approx 0.0 \pm 0.15$ (Figure 4). Unlike Thevenin & Jasiewicz (1997), we do not find any significant barium enhancement.
2. The white dwarf parameters: Combining astrometry and UV spectroscopy, we find the WD radius to lie in the range of $\approx (1.75 \pm 0.25) \times 10^{-2} R_{\odot}$. We show this to be in tension with the spectroscopic $\log(g) = 7.2 \pm 0.3$ and temperature (80 ± 10 kK) estimated in Ziegler et al. (2012), as there is no consistent solution as per the post-AGB models of Miller Bertolami (2016). Allowing for higher $\log(g)$ (as in Herald & Bianchi 2002) can yield a possible solution at $M_{\text{WD}} \gtrsim 0.57 M_{\odot}$ (Figure 5, left panel).
3. Comparison of the Gaia astrometry-allowed subgiant masses to a range of initial masses of the WD shows that it is unlikely that the subgiant is a naturally evolved star (Figure 6). This favors the scenario of the subgiant being a temporarily inflated main sequence star.
4. Gaia astrometry shows that A35 is the inner binary of a hierarchical triple system, with the tertiary being a K dwarf at a distance of ≈ 1600 AU. Though its influence is negligible today, it may have played a significant role in the past in bringing the inner binary to its current configuration and triggering mass transfer.

Our primary results from the MESA binary models are as follows:

1. We use a new accretion prescription where we use realistic relations for the energy, density, and pressure

- of the in-falling material (Equation 2). This is expected to capture the entropy deposited on the accretor better than the fiducial MESA setup, especially at high accretion rates. This prescription allowed us to evolve both stars in MESA binary simulations self-consistently through RGB/AGB mass transfer phases even for high initial donor to accretor mass ratios.
2. The accretor inflates significantly during mass transfer. For example, a $0.5 M_{\odot}$ accretor achieves a peak radius of $\approx 80 R_{\odot}$ during the phase of highest \dot{M} (Figure 7). However, it doesn't fill its Roche lobe, contrary to what is commonly assumed for inflated companions. Post-mass transfer, the inflated accretor begins to thermally relax back to main sequence. It remains significantly inflated for at least the next million years (i.e., comparable to its thermal timescale).
 3. The phase of thermal relaxation meets the parameters of the A35-type systems reasonably well at a post-mass transfer age of $10^4 - 10^6$ years (Figures 8 and 11). Additionally, we present other post-mass transfer systems, namely the post-AGB binaries, the Blue Lurkers, and the broader population of WD+main sequence binaries as representing different stages of the same evolutionary pathway (Figure 13).

4. The primary prediction from our models is that most AU-scale companions to hot (cold) WDs should be inflated (normal main sequence) stars. This can be tested through optical and UV follow-ups of binaries with a WD, usually selected through UV excess or being located inside PNe.

5. ACKNOWLEDGMENTS

S.B. thanks David Jones for reading the manuscript and providing comments. This research was supported by NSF grants AST-2508988 and AST-2307232. C.S. acknowledges support from the Department of Energy Computational Science Graduate Fellowship, supported by the U.S. Department of Energy, Office of Science, Office of Advanced Scientific Computing Research, under Award Number DE-SC0026073. We have used the Python packages Numpy (Harris et al. 2020), SciPy (Virtanen et al. 2020), Matplotlib (Hunter 2007), Pandas (pandas development team 2020), Astropy (Astropy Collaboration et al. 2013, 2018), and Astropyquery (Ginsburg et al. 2019) at various stages of this research.

6. DATA AVAILABILITY

All the relevant codes to reproduce the results of this paper can be found in https://github.com/Soumin1908/InflatedStars_A35_MesaModels.git

APPENDIX

A. THE POSSIBLE DYNAMICAL ROLE OF THE TERTIARY

Hierarchical triples are common in the Galactic field (e.g., Raghavan et al. 2010; Tokovinin 2014; Moe & Di Stefano 2017; Winters et al. 2019; Moe & Kratter 2021; Offner et al. 2023; Shariat et al. 2025a) and play a key an important role in the formation and evolution of post-mass-transfer WD+main sequence binaries such as A35 (e.g., Toonen et al. 2016, 2020, 2022; Knigge et al. 2022; Rajamuthukumar et al. 2023, 2025; Hallakoun et al. 2024; Shariat et al. 2023, 2025b,c,d; Perets 2025). In particular, if the inner binary formed on a relatively wide orbit ($\gtrsim 10$ au), secular perturbations from the tertiary would have driven oscillations to the inner binary's eccentricity and inclination through the eccentric Kozai-Lidov mechanism (Kozai 1962; Lidov 1962; Naoz 2016). At fixed semi-major axis, these eccentricity oscillations amount to oscillations in the periastron distance of the inner binary. As the primary evolves onto the giant branch and its radius increases, close periastron passages allow tides to efficiently dissipate orbital energy, causing the orbit to circularize and shrink. Since the tidal synchronization timescale for equilibrium tides depends steeply on stellar radius ($\propto R^6$; Zahn 1977), the most likely mass-transfer outcome is that the inner-binary interaction begins when the primary is on the late RGB or AGB (e.g., Toonen et al. 2020; Shariat et al. 2025b,d). At this stage, the tertiary's gravitational influence is negligible, and the inner binary evolves effectively in isola-

tion, allowing stable mass transfer and the subsequent binary evolution to proceed.

Overall, the primary role of hierarchical triples in A35-like systems is to increase the fraction of binaries that experience mass transfer by enabling close periastron passages in binaries that would otherwise remain too wide ($\gtrsim 10$ au) to interact in isolation. The detailed binary evolution calculations presented in Section 3 are agnostic to the pre-mass-transfer history of the system. Nevertheless, tertiary companions may be common and astrophysically important to the formation of A35-like systems today. Note that some tertiaries may no longer be bound due to sudden mass loss either during mass transfer or late-AGB mass loss in the inner binary (e.g., El-Badry & Rix 2018; Igoshev et al. 2020; Shariat et al. 2023; Hwang & Zakamska 2025; O'Connor 2025), while others may have evolved into faint white dwarfs that are challenging to detect observationally. Future systematic searches for tertiaries around post-mass-transfer WD+main sequence binaries, particularly in PNe, will be essential for quantifying their occurrence, separations, and evolutionary role.

B. COMPANION MASS FROM GAIA ASTROMETRY

The six astrometric parameters provided by Gaia are relevant for this calculation are: the parallax, ϖ , the orbital period, P_{orb} , and the four Thiele-Innes (TI) elements A , B , F , and G_T (to distinguish from the gravitational constant). We define $P = A^2 + B^2 + F^2 + G_T^2$ and $Q = AG_T - BF$. From the definition of the TI elements, it is then easy to show that

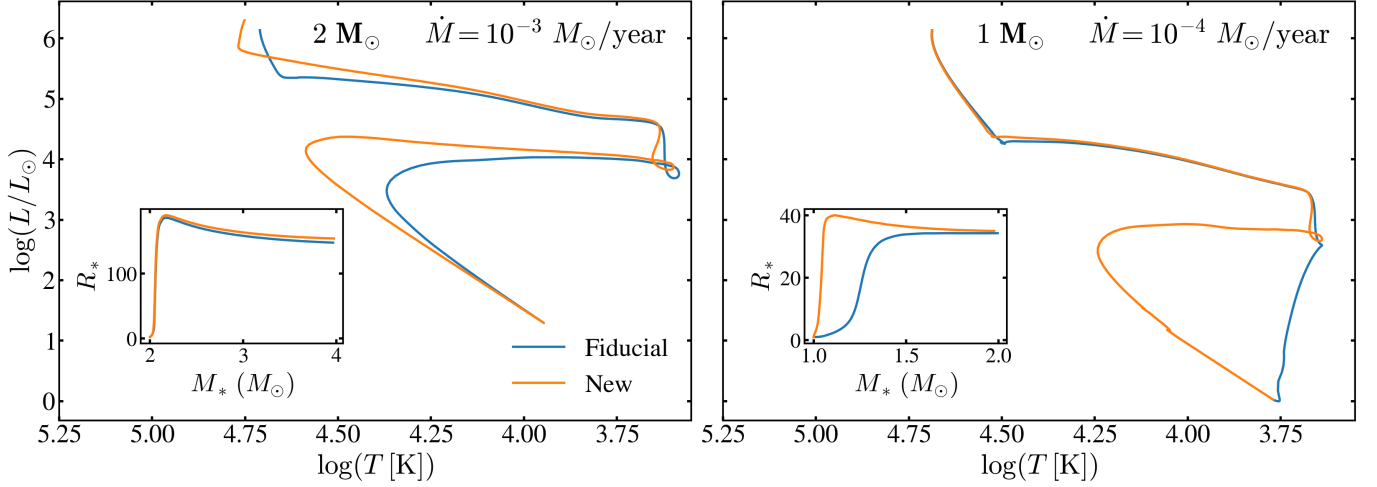


Figure 15. Evolution of a $2 M_{\odot}$ accretor with $\dot{M} = 10^{-3} M_{\odot}/\text{year}$ (left panel) and $1 M_{\odot}$ accretor with $\dot{M} = 10^{-4} M_{\odot}/\text{year}$ (right panel) for the fiducial and new accretion prescriptions. The insets show the evolution of the accretor radius until its mass doubles. The dotted line in the right panel denotes the portion in the HR diagram before attaining the Hayashi limit where the convective mass fraction in the ‘outer half’ ($R > 0.5 R_{\odot}$) of the star is $< 10^{-2}$. Unlike the fiducial case, the added entropy in the new accretion prescription disrupts the convective envelopes of low-mass stars at early stages, thus mimicking the evolution of high-mass stars.

the orbital inclination is given by:

$$\cos(i) = \frac{P - \sqrt{P^2 - 4Q^2}}{2Q}, \quad (\text{B1})$$

which yields a corresponding semi-major axis of the Gaia photo-center:

$$a_{\text{pc}} = \sqrt{\frac{Q}{\cos(i)}} \frac{1}{\varpi}. \quad (\text{B2})$$

With a WD to subgiant Gaia G-band flux ratio of $\epsilon = F_{G, \text{WD}}/F_{G, \text{SG}}$, this yields a binary semi-major axis as:

$$a = a_{\text{pc}} \left(\frac{M_{\text{WD}}}{M_{\text{SG}} + M_{\text{WD}}} - \frac{\epsilon}{1 + \epsilon} \right)^{-1}. \quad (\text{B3})$$

We solve this consistently with Kepler’s third law to calculate M_{SG} for a given M_{WD} .

C. COMPARISON WITH THE ‘HAMSTARS’

Recently [Lau et al. \(2024\)](#) conducted a systematic study of inflation of accreting stars of masses $> 2 M_{\odot}$. They assumed a constant accretion rate, and continued accretion until the total mass of the accretor becomes $100 M_{\odot}$. They also employed the fiducial MESA accretion prescription of the accreting material being of the same physical properties of the stellar photosphere. They call their systems ‘Hamstars’ for their systems are objects which swallow mass and inflate.

Apart from the difference in the accretion prescription used, the other major difference with this work is the range of stellar masses of interest. The mass range investigated in [Lau et al. \(2024\)](#) have radiative envelopes. Whereas, this work explores the mass $\lesssim 1 M_{\odot}$, which has a convective envelope. This can potentially lead to a substantial difference in their reaction to accretion. This is because, convective polytropes

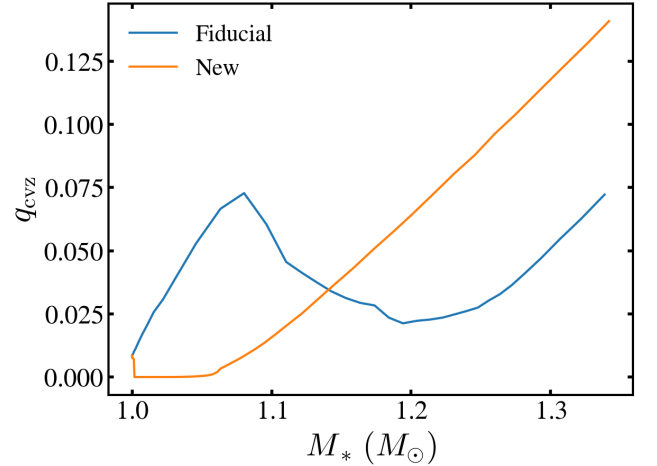


Figure 16. Mass fraction of the surface convection zone (calculated from the Ledoux unstable mass at radius $> 0.5 R_{\odot}$) as a function of the total mass for the $1 M_{\odot}$ accretor for both accretion prescriptions. The new prescription disrupts surface convection almost completely at the very initial stages of accretion.

tend to prevent the expansion of the star, whereas radiative envelopes tend to expand on accretion. This was recently investigated by [Zhao et al. \(2024\)](#).

We discuss here how our new accretion prescription affect the response of the accretor. We do this by taking a $1 M_{\odot}$ and $2 M_{\odot}$ star and conducting the exercise as in [Lau et al. \(2024\)](#): adopt a constant \dot{M} for a long duration. For demonstration, we choose $\dot{M} = 10^{-4} M_{\odot}/\text{year}$ and $\dot{M} = 10^{-3} M_{\odot}/\text{year}$ respectively for the two stellar masses. We ramp up the accretion rate to the adopted value over a duration such that a net of $0.1 M_{\odot}$ is accreted during this phase. We checked that

our results are not affected with the change in the ramp-up duration.

The results are shown in Figure 15, where we present the evolution of the accretor in the Hertzsprung-Russel diagram (HRD) and the change in stellar radius as a function of mass (till the mass is doubled) as insets. We first discuss the case of the $2 M_{\odot}$ star which has a radiative envelope. For the fiducial prescription of MESA (thermodynamic properties of the accreted material being the same as stellar surface), we recover the tracks presented in Lau et al. (2024). But with the new prescription, we see that the star becomes much brighter compared to the fiducial case before approaching the Hayashi limit, after which the evolution is nearly identical. This is primarily caused by a higher temperature which results from the higher accretion energy in the new prescription. However, the radius evolution stays nearly identical throughout. Why this is the case is unclear.

The case of the $1 M_{\odot}$ star, however, is very different – the HRD tracks for the two prescriptions differ significantly. This is accompanied by a substantial difference in radius evolution, where we see that with the new prescription, the

star undergoes a rapid expansion at the very early stages of the mass transfer. Interestingly, this behavior is qualitatively similar to that of the $2 M_{\odot}$ star. Inspection shows that the envelope properties of the low mass star evolves differently with the two prescriptions (Figure 16). In the fiducial case, the added mass bears the same entropy as the stellar surface. Thus, the envelope remains convective. This makes the star evolve similar to a convective star, and it almost follows the Hayashi track from the beginning. With the new prescription, however, the entropy of the added material is much higher than that of the stellar surface. This quickly disrupts the surface convection, making the star behave qualitatively similarly to a radiative-envelope star. Once it reaches the Hayashi limit, the two tracks converge and the subsequent evolution is nearly identical.

This exercise demonstrates the importance of properly considering the accretion entropy deposited on the stellar evolution, especially for low mass stars. We deem this particularly important for close mass transfer binaries, where a quick initial expansion of the accretor can result in an early CE. This motivates future work to quantify the effect more accurately.

REFERENCES

- Abell, G. O. 1955, *PASP*, 67, 258, doi: [10.1086/126815](https://doi.org/10.1086/126815)
- Aller, A., Lillo-Box, J., Vučković, M., et al. 2018, *MNRAS*, 476, 1140, doi: [10.1093/mnras/sty174](https://doi.org/10.1093/mnras/sty174)
- Andrae, R., Fouesneau, M., Sordo, R., et al. 2023, *A&A*, 674, A27, doi: [10.1051/0004-6361/202243462](https://doi.org/10.1051/0004-6361/202243462)
- Astropy Collaboration, Robitaille, T. P., Tollerud, E. J., et al. 2013, *A&A*, 558, A33, doi: [10.1051/0004-6361/201322068](https://doi.org/10.1051/0004-6361/201322068)
- Astropy Collaboration, Price-Whelan, A. M., Sipőcz, B. M., et al. 2018, *AJ*, 156, 123, doi: [10.3847/1538-3881/aabc4f](https://doi.org/10.3847/1538-3881/aabc4f)
- Belloni, D., Schreiber, M. R., & Zorotovic, M. 2024, *A&A*, 687, A12, doi: [10.1051/0004-6361/202449320](https://doi.org/10.1051/0004-6361/202449320)
- Bhattacharjee, S., Kulkarni, S. R., Kong, A. K. H., et al. 2025, *PASP*, 137, 024201, doi: [10.1088/1538-3873/ada702](https://doi.org/10.1088/1538-3873/ada702)
- Blanco-Cuaresma, S. 2019, *MNRAS*, 486, 2075, doi: [10.1093/mnras/stz549](https://doi.org/10.1093/mnras/stz549)
- Blanco-Cuaresma, S., Soubiran, C., Heiter, U., & Jofré, P. 2014, *A&A*, 569, A111, doi: [10.1051/0004-6361/201423945](https://doi.org/10.1051/0004-6361/201423945)
- Bloecker, T. 1995, *A&A*, 297, 727
- Bohlin, R. C., Mészáros, S., Fleming, S. W., et al. 2017, *AJ*, 153, 234, doi: [10.3847/1538-3881/aa6ba9](https://doi.org/10.3847/1538-3881/aa6ba9)
- Bond, H. E., & Livio, M. 1990, *ApJ*, 355, 568, doi: [10.1086/168789](https://doi.org/10.1086/168789)
- Bond, H. E., & Zeimann, G. R. 2024, *ApJ*, 967, 122, doi: [10.3847/1538-4357/ad3df9](https://doi.org/10.3847/1538-4357/ad3df9)
- Brahm, R., Jordán, A., & Espinoza, N. 2017, *PASP*, 129, 034002, doi: [10.1088/1538-3873/aa5455](https://doi.org/10.1088/1538-3873/aa5455)
- Budaj, J., Bernhard, K., Jones, D., & Munday, J. 2025, *Nature Astronomy*, 9, 380, doi: [10.1038/s41550-024-02446-x](https://doi.org/10.1038/s41550-024-02446-x)
- Buder, S., Kos, J., Wang, X. E., et al. 2025, *PASA*, 42, e051, doi: [10.1017/pasa.2025.26](https://doi.org/10.1017/pasa.2025.26)
- Choi, J., Dotter, A., Conroy, C., et al. 2016, *ApJ*, 823, 102, doi: [10.3847/0004-637X/823/2/102](https://doi.org/10.3847/0004-637X/823/2/102)
- Cox, J. P., & Giuli, R. T. 1968, *Principles of stellar structure*
- Cunningham, T., Tremblay, P.-E., & W. O'Brien, M. 2024, *MNRAS*, 527, 3602, doi: [10.1093/mnras/stad3275](https://doi.org/10.1093/mnras/stad3275)
- Declair, M., Gordon, K. D., Andrews, J. E., et al. 2022, *ApJ*, 930, 15, doi: [10.3847/1538-4357/ac5dbb](https://doi.org/10.3847/1538-4357/ac5dbb)
- Dorman, B., Rood, R. T., & O'Connell, R. W. 1993, *ApJ*, 419, 596, doi: [10.1086/173511](https://doi.org/10.1086/173511)
- Dotter, A. 2016, *ApJS*, 222, 8, doi: [10.3847/0067-0049/222/1/8](https://doi.org/10.3847/0067-0049/222/1/8)
- El-Badry, K. 2025, *The Open Journal of Astrophysics*, 8, 62, doi: [10.33232/001c.138448](https://doi.org/10.33232/001c.138448)
- El-Badry, K., & Rix, H.-W. 2018, *Monthly Notices of the Royal Astronomical Society*, 480, 4884, doi: [10.1093/mnras/sty2186](https://doi.org/10.1093/mnras/sty2186)
- El-Badry, K., Seeburger, R., Jayasinghe, T., et al. 2022, *MNRAS*, 512, 5620, doi: [10.1093/mnras/stac815](https://doi.org/10.1093/mnras/stac815)
- Fitzpatrick, E. L., Massa, D., Gordon, K. D., Bohlin, R., & Clayton, G. C. 2019, *ApJ*, 886, 108, doi: [10.3847/1538-4357/ab4c3a](https://doi.org/10.3847/1538-4357/ab4c3a)
- Foreman-Mackey, D., Hogg, D. W., Lang, D., & Goodman, J. 2013, *PASP*, 125, 306, doi: [10.1086/670067](https://doi.org/10.1086/670067)
- Fujimoto, M. Y., & Iben, Jr., I. 1989, *ApJ*, 341, 306, doi: [10.1086/167495](https://doi.org/10.1086/167495)
- Gaia Collaboration, Montegriffo, P., Bellazzini, M., et al. 2023, *A&A*, 674, A33, doi: [10.1051/0004-6361/202243709](https://doi.org/10.1051/0004-6361/202243709)

- Garbutt, J. A., Parsons, S. G., Toloza, O., et al. 2024, *MNRAS*, 529, 4840, doi: [10.1093/mnras/stae807](https://doi.org/10.1093/mnras/stae807)
- Gatti, A. A., Drew, J. E., Oudmaijer, R. D., Marsh, T. R., & Lynas-Gray, A. E. 1998, *MNRAS*, 301, L33, doi: [10.48550/arXiv.astro-ph/9809331](https://doi.org/10.48550/arXiv.astro-ph/9809331)
- Ge, H., Webbink, R. F., Chen, X., & Han, Z. 2020, *ApJ*, 899, 132, doi: [10.3847/1538-4357/aba7b7](https://doi.org/10.3847/1538-4357/aba7b7)
- Ginsburg, A., Sipőcz, B. M., Basseur, C. E., et al. 2019, *AJ*, 157, 98, doi: [10.3847/1538-3881/aafc33](https://doi.org/10.3847/1538-3881/aafc33)
- Gordon, K. 2024a, *dust_extinction: Interstellar Dust Extinction Models*, v1.5, Zenodo, doi: [10.5281/zenodo.4658887](https://doi.org/10.5281/zenodo.4658887)
- . 2024b, *The Journal of Open Source Software*, 9, 7023, doi: [10.21105/joss.07023](https://doi.org/10.21105/joss.07023)
- Gordon, K. D., Cartledge, S., & Clayton, G. C. 2009, *ApJ*, 705, 1320, doi: [10.1088/0004-637X/705/2/1320](https://doi.org/10.1088/0004-637X/705/2/1320)
- Gordon, K. D., Clayton, G. C., Declair, M., et al. 2023, *ApJ*, 950, 86, doi: [10.3847/1538-4357/accb59](https://doi.org/10.3847/1538-4357/accb59)
- Gordon, K. D., Misselt, K. A., Bouwman, J., et al. 2021, *ApJ*, 916, 33, doi: [10.3847/1538-4357/ac00b7](https://doi.org/10.3847/1538-4357/ac00b7)
- Gossage, S., Kalogera, V., & Sun, M. 2023, *ApJ*, 950, 27, doi: [10.3847/1538-4357/acc86e](https://doi.org/10.3847/1538-4357/acc86e)
- Gray, R. O., & Corbally, C. J. 1994, *AJ*, 107, 742, doi: [10.1086/116893](https://doi.org/10.1086/116893)
- Green, G. M., Schlafly, E., Zucker, C., Speagle, J. S., & Finkbeiner, D. 2019, *ApJ*, 887, 93, doi: [10.3847/1538-4357/ab5362](https://doi.org/10.3847/1538-4357/ab5362)
- Hallakoun, N., Shahaf, S., Mazeh, T., Toonen, S., & Ben-Ami, S. 2024, *ApJL*, 970, L11, doi: [10.3847/2041-8213/ad5e63](https://doi.org/10.3847/2041-8213/ad5e63)
- Han, Z., Podsiadlowski, P., Maxted, P. F. L., & Marsh, T. R. 2003, *MNRAS*, 341, 669, doi: [10.1046/j.1365-8711.2003.06451.x](https://doi.org/10.1046/j.1365-8711.2003.06451.x)
- Harris, C. R., Millman, K. J., van der Walt, S. J., et al. 2020, *Nature*, 585, 357, doi: [10.1038/s41586-020-2649-2](https://doi.org/10.1038/s41586-020-2649-2)
- Herald, J. E., & Bianchi, L. 2002, *ApJ*, 580, 434, doi: [10.1086/343034](https://doi.org/10.1086/343034)
- Hillen, M., Kluska, J., Le Bouquin, J.-B., et al. 2016, *A&A*, 588, L1, doi: [10.1051/0004-6361/201628125](https://doi.org/10.1051/0004-6361/201628125)
- Hunter, J. D. 2007, *Computing in Science & Engineering*, 9, 90, doi: [10.1109/MCSE.2007.55](https://doi.org/10.1109/MCSE.2007.55)
- Husser, T.-O., Wende-von Berg, S., Dreizler, S., et al. 2013, *A&A*, 553, A6, doi: [10.1051/0004-6361/201219058](https://doi.org/10.1051/0004-6361/201219058)
- Hwang, H.-C., & Zakamska, N. L. 2025, *ApJ*, 991, 226, doi: [10.3847/1538-4357/adfa1c](https://doi.org/10.3847/1538-4357/adfa1c)
- Igoshev, A. P., Perets, H. B., & Michaely, E. 2020, *MNRAS*, 494, 1448, doi: [10.1093/mnras/staa833](https://doi.org/10.1093/mnras/staa833)
- Ironi, O., Ben-Ami, S., Hallakoun, N., & Shahaf, S. 2025, *ApJ*, 982, 20, doi: [10.3847/1538-4357/adb5f2](https://doi.org/10.3847/1538-4357/adb5f2)
- Ivanova, N., Justham, S., Chen, X., et al. 2013, *A&A Rv*, 21, 59, doi: [10.1007/s00159-013-0059-2](https://doi.org/10.1007/s00159-013-0059-2)
- Jacoby, G. H. 1981, *ApJ*, 244, 903, doi: [10.1086/158765](https://doi.org/10.1086/158765)
- Jayasinghe, T., Thompson, T. A., Kochanek, C. S., et al. 2022, *MNRAS*, 516, 5945, doi: [10.1093/mnras/stac2187](https://doi.org/10.1093/mnras/stac2187)
- Johnson, J. A., Petigura, E. A., Fulton, B. J., et al. 2017, *AJ*, 154, 108, doi: [10.3847/1538-3881/aa80e7](https://doi.org/10.3847/1538-3881/aa80e7)
- Jones, D. 2020, in *Reviews in Frontiers of Modern Astrophysics; From Space Debris to Cosmology*, 123–153, doi: [10.1007/978-3-030-38509-5_5](https://doi.org/10.1007/978-3-030-38509-5_5)
- Jones, D., Boffin, H. M. J., Brown, A. J., et al. 2022, *MNRAS*, 516, 4833, doi: [10.1093/mnras/stac2501](https://doi.org/10.1093/mnras/stac2501)
- Jones, D., Van Winckel, H., Aller, A., Exter, K., & De Marco, O. 2017, *A&A*, 600, L9, doi: [10.1051/0004-6361/201730700](https://doi.org/10.1051/0004-6361/201730700)
- Jorissen, A., Frankowski, A., Famaey, B., & van Eck, S. 2009, *A&A*, 498, 489, doi: [10.1051/0004-6361/200810703](https://doi.org/10.1051/0004-6361/200810703)
- Kaufer, A., Stahl, O., Tubbesing, S., et al. 1999, *The Messenger*, 95, 8
- Kawahara, H., Masuda, K., MacLeod, M., et al. 2018, *AJ*, 155, 144, doi: [10.3847/1538-3881/aaaaaf](https://doi.org/10.3847/1538-3881/aaaaaf)
- Kippenhahn, R., & Meyer-Hofmeister, E. 1977, *A&A*, 54, 539
- Knigge, C., Toonen, S., & Boekholt, T. C. N. 2022, *MNRAS*, 514, 1895, doi: [10.1093/mnras/stac1336](https://doi.org/10.1093/mnras/stac1336)
- Kolb, U., & Ritter, H. 1990, *A&A*, 236, 385
- Kozai, Y. 1962, *AJ*, 67, 591, doi: [10.1086/108790](https://doi.org/10.1086/108790)
- Kruse, E., & Agol, E. 2014, *Science*, 344, 275, doi: [10.1126/science.1251999](https://doi.org/10.1126/science.1251999)
- Lau, M. Y. M., Hirai, R., Mandel, I., & Tout, C. A. 2024, *ApJL*, 966, L7, doi: [10.3847/2041-8213/ad3d50](https://doi.org/10.3847/2041-8213/ad3d50)
- Ledoux, P. 1947, *ApJ*, 105, 305, doi: [10.1086/144905](https://doi.org/10.1086/144905)
- Leiner, E., Mathieu, R. D., Vanderburg, A., Gosnell, N. M., & Smith, J. C. 2019, *ApJ*, 881, 47, doi: [10.3847/1538-4357/ab2bf8](https://doi.org/10.3847/1538-4357/ab2bf8)
- Leiner, E. M., Gosnell, N. M., Geller, A. M., et al. 2025, *ApJL*, 979, L1, doi: [10.3847/2041-8213/ad9d0c](https://doi.org/10.3847/2041-8213/ad9d0c)
- Li, Z., Chen, X., Chen, H.-L., & Han, Z. 2019, *ApJ*, 871, 148, doi: [10.3847/1538-4357/aaf9a1](https://doi.org/10.3847/1538-4357/aaf9a1)
- Lidov, M. L. 1962, *Planet. Space Sci.*, 9, 719, doi: [10.1016/0032-0633\(62\)90129-0](https://doi.org/10.1016/0032-0633(62)90129-0)
- Löbbling, L., Boffin, H. M. J., & Jones, D. 2019, *A&A*, 624, A1, doi: [10.1051/0004-6361/201834466](https://doi.org/10.1051/0004-6361/201834466)
- Löbbling, L., Maney, M. A., Rauch, T., et al. 2020, *MNRAS*, 492, 528, doi: [10.1093/mnras/stz3247](https://doi.org/10.1093/mnras/stz3247)
- Lu, W., Fuller, J., Quataert, E., & Bonnerot, C. 2023, *MNRAS*, 519, 1409, doi: [10.1093/mnras/stac3621](https://doi.org/10.1093/mnras/stac3621)
- Masuda, K., Kawahara, H., Latham, D. W., et al. 2019, *ApJL*, 881, L3, doi: [10.3847/2041-8213/ab321b](https://doi.org/10.3847/2041-8213/ab321b)
- Mészáros, S., Bohlin, R., Allende Prieto, C., et al. 2024, *A&A*, 688, A197, doi: [10.1051/0004-6361/202449306](https://doi.org/10.1051/0004-6361/202449306)
- Meyer, F., & Meyer-Hofmeister, E. 1979, *A&A*, 78, 167
- Miller Bertolami, M. M. 2016, *A&A*, 588, A25, doi: [10.1051/0004-6361/201526577](https://doi.org/10.1051/0004-6361/201526577)
- Moe, M., & Di Stefano, R. 2017, *ApJS*, 230, 15, doi: [10.3847/1538-4365/aa6fb6](https://doi.org/10.3847/1538-4365/aa6fb6)
- Moe, M., & Kratter, K. M. 2021, *MNRAS*, 507, 3593, doi: [10.1093/mnras/stab2328](https://doi.org/10.1093/mnras/stab2328)

- Nagarajan, P., & El-Badry, K. 2024, *PASP*, 136, 094203, doi: [10.1088/1538-3873/ad7981](https://doi.org/10.1088/1538-3873/ad7981)
- Naoz, S. 2016, *ARA&A*, 54, 441, doi: [10.1146/annurev-astro-081915-023315](https://doi.org/10.1146/annurev-astro-081915-023315)
- Neo, S., Miyaji, S., Nomoto, K., & Sugimoto, D. 1977a, *PASJ*, 29, 249, doi: [10.1093/pasj/29.2.249](https://doi.org/10.1093/pasj/29.2.249)
- . 1977b, *PASJ*, 29, 249, doi: [10.1093/pasj/29.2.249](https://doi.org/10.1093/pasj/29.2.249)
- Nine, A. C., Mathieu, R. D., Gosnell, N. M., & Leiner, E. M. 2023, *ApJ*, 944, 145, doi: [10.3847/1538-4357/acb046](https://doi.org/10.3847/1538-4357/acb046)
- O'Connor, C. E. 2025, arXiv e-prints, arXiv:2509.08880, doi: [10.48550/arXiv.2509.08880](https://doi.org/10.48550/arXiv.2509.08880)
- Offner, S. S. R., Moe, M., Kratter, K. M., et al. 2023, in *Astronomical Society of the Pacific Conference Series*, Vol. 534, *Protostars and Planets VII*, ed. S. Inutsuka, Y. Aikawa, T. Muto, K. Tomida, & M. Tamura, 275, doi: [10.48550/arXiv.2203.10066](https://doi.org/10.48550/arXiv.2203.10066)
- Oomen, G.-M., Van Winckel, H., Pols, O., et al. 2018, *A&A*, 620, A85, doi: [10.1051/0004-6361/201833816](https://doi.org/10.1051/0004-6361/201833816)
- Packet, W. 1981, *A&A*, 102, 17
- pandas development team, T. 2020, *pandas-dev/pandas: Pandas, latest*, Zenodo, doi: [10.5281/zenodo.3509134](https://doi.org/10.5281/zenodo.3509134)
- Parsons, S. G., Rebassa-Mansergas, A., Schreiber, M. R., et al. 2016, *MNRAS*, 463, 2125, doi: [10.1093/mnras/stw2143](https://doi.org/10.1093/mnras/stw2143)
- Paxton, B., Bildsten, L., Dotter, A., et al. 2011, *ApJS*, 192, 3, doi: [10.1088/0067-0049/192/1/3](https://doi.org/10.1088/0067-0049/192/1/3)
- Paxton, B., Marchant, P., Schwab, J., et al. 2015, *ApJS*, 220, 15, doi: [10.1088/0067-0049/220/1/15](https://doi.org/10.1088/0067-0049/220/1/15)
- Paxton, B., Smolec, R., Schwab, J., et al. 2019, *ApJS*, 243, 10, doi: [10.3847/1538-4365/ab2241](https://doi.org/10.3847/1538-4365/ab2241)
- Perets, H. B. 2025, arXiv e-prints, arXiv:2504.02939, doi: [10.48550/arXiv.2504.02939](https://doi.org/10.48550/arXiv.2504.02939)
- Perryman, M. A. C., Lindegren, L., Kovalevsky, J., et al. 1997, *A&A*, 323, L49
- Petigura, E. A., Howard, A. W., Marcy, G. W., et al. 2017, *AJ*, 154, 107, doi: [10.3847/1538-3881/aa80de](https://doi.org/10.3847/1538-3881/aa80de)
- Popham, R., & Narayan, R. 1991, *ApJ*, 370, 604, doi: [10.1086/169847](https://doi.org/10.1086/169847)
- Poznanski, D., Prochaska, J. X., & Bloom, J. S. 2012, *MNRAS*, 426, 1465, doi: [10.1111/j.1365-2966.2012.21796.x](https://doi.org/10.1111/j.1365-2966.2012.21796.x)
- Raghavan, D., McAlister, H. A., Henry, T. J., et al. 2010, *ApJS*, 190, 1, doi: [10.1088/0067-0049/190/1/1](https://doi.org/10.1088/0067-0049/190/1/1)
- Rajamuthukumar, A. S., Hamers, A. S., Neunteufel, P., Pakmor, R., & de Mink, S. E. 2023, *ApJ*, 950, 9, doi: [10.3847/1538-4357/acc86c](https://doi.org/10.3847/1538-4357/acc86c)
- Rajamuthukumar, A. S., Korol, V., Stegmann, J., et al. 2025, arXiv e-prints, arXiv:2502.09607, doi: [10.48550/arXiv.2502.09607](https://doi.org/10.48550/arXiv.2502.09607)
- Rappaport, S., Podsiadlowski, P., Joss, P. C., Di Stefano, R., & Han, Z. 1995, *MNRAS*, 273, 731, doi: [10.1093/mnras/273.3.731](https://doi.org/10.1093/mnras/273.3.731)
- Rappaport, S., Verbunt, F., & Joss, P. C. 1983, *ApJ*, 275, 713, doi: [10.1086/161569](https://doi.org/10.1086/161569)
- Rauch, T., & Deetjen, J. L. 2003, in *Astronomical Society of the Pacific Conference Series*, Vol. 288, *Stellar Atmosphere Modeling*, ed. I. Hubeny, D. Mihalas, & K. Werner, 103, doi: [10.48550/arXiv.astro-ph/0403239](https://doi.org/10.48550/arXiv.astro-ph/0403239)
- Rebassa-Mansergas, A., Gänsicke, B. T., Rodríguez-Gil, P., Schreiber, M. R., & Koester, D. 2007, *MNRAS*, 382, 1377, doi: [10.1111/j.1365-2966.2007.12288.x](https://doi.org/10.1111/j.1365-2966.2007.12288.x)
- Reimers, D. 1975, *Memoires of the Societe Royale des Sciences de Liege*, 8, 369
- Reyniers, M., & Van Winckel, H. 2001, *A&A*, 365, 465, doi: [10.1051/0004-6361:20000146](https://doi.org/10.1051/0004-6361:20000146)
- Scherbak, P., Lu, W., & Fuller, J. 2025, *ApJ*, 990, 172, doi: [10.3847/1538-4357/adf067](https://doi.org/10.3847/1538-4357/adf067)
- Shahaf, S. 2025, *ApJ*, 981, 54, doi: [10.3847/1538-4357/adb156](https://doi.org/10.3847/1538-4357/adb156)
- Shahaf, S., Bashi, D., Mazeh, T., et al. 2023, *MNRAS*, 518, 2991, doi: [10.1093/mnras/stac3290](https://doi.org/10.1093/mnras/stac3290)
- Shariat, C., El-Badry, K., & Naoz, S. 2025a, *PASP*, 137, 094201, doi: [10.1088/1538-3873/adfb30](https://doi.org/10.1088/1538-3873/adfb30)
- Shariat, C., El-Badry, K., Naoz, S., Rodriguez, A. C., & van Roestel, J. 2025b, *PASP*, 137, 074201, doi: [10.1088/1538-3873/add5a1](https://doi.org/10.1088/1538-3873/add5a1)
- Shariat, C., Naoz, S., El-Badry, K., et al. 2025c, *ApJ*, 978, 47, doi: [10.3847/1538-4357/ad944a](https://doi.org/10.3847/1538-4357/ad944a)
- Shariat, C., Naoz, S., Hansen, B. M. S., et al. 2023, *ApJL*, 955, L14, doi: [10.3847/2041-8213/acf76b](https://doi.org/10.3847/2041-8213/acf76b)
- Shariat, C., Ye, C. S., Naoz, S., & Rose, S. 2025d, arXiv e-prints, arXiv:2511.18678, doi: [10.48550/arXiv.2511.18678](https://doi.org/10.48550/arXiv.2511.18678)
- Sheinis, A., Anguiano, B., Asplund, M., et al. 2015, *Journal of Astronomical Telescopes, Instruments, and Systems*, 1, 035002, doi: [10.1117/1.JATIS.1.3.035002](https://doi.org/10.1117/1.JATIS.1.3.035002)
- Soberman, G. E., Phinney, E. S., & van den Heuvel, E. P. J. 1997, *A&A*, 327, 620, doi: [10.48550/arXiv.astro-ph/9703016](https://doi.org/10.48550/arXiv.astro-ph/9703016)
- Sun, M., & Arras, P. 2018, *ApJ*, 858, 14, doi: [10.3847/1538-4357/aab9a4](https://doi.org/10.3847/1538-4357/aab9a4)
- Temmink, K. D., Pols, O. R., Justham, S., Istrate, A. G., & Toonen, S. 2023, *A&A*, 669, A45, doi: [10.1051/0004-6361/202244137](https://doi.org/10.1051/0004-6361/202244137)
- Thevenin, F., & Jasniewicz, G. 1997, *A&A*, 320, 913
- Tokovinin, A. 2014, *AJ*, 147, 86, doi: [10.1088/0004-6256/147/4/86](https://doi.org/10.1088/0004-6256/147/4/86)
- Toonen, S., Boekholt, T. C. N., & Portegies Zwart, S. 2022, *A&A*, 661, A61, doi: [10.1051/0004-6361/202141991](https://doi.org/10.1051/0004-6361/202141991)
- Toonen, S., Hamers, A., & Portegies Zwart, S. 2016, *Computational Astrophysics and Cosmology*, 3, 6, doi: [10.1186/s40668-016-0019-0](https://doi.org/10.1186/s40668-016-0019-0)
- Toonen, S., Portegies Zwart, S., Hamers, A. S., & Bandopadhyay, D. 2020, *A&A*, 640, A16, doi: [10.1051/0004-6361/201936835](https://doi.org/10.1051/0004-6361/201936835)
- Tyndall, A. A., Jones, D., Boffin, H. M. J., et al. 2013, *MNRAS*, 436, 2082, doi: [10.1093/mnras/stt1713](https://doi.org/10.1093/mnras/stt1713)
- van Winckel, H. 2003, *ARA&A*, 41, 391, doi: [10.1146/annurev.astro.41.071601.170018](https://doi.org/10.1146/annurev.astro.41.071601.170018)

- Van Winckel, H., Jorissen, A., Exter, K., et al. 2014, *A&A*, 563, L10, doi: [10.1051/0004-6361/201423650](https://doi.org/10.1051/0004-6361/201423650)
- Verhoelst, T., van Aarle, E., & Acke, B. 2007, *A&A*, 470, L21, doi: [10.1051/0004-6361:20077840](https://doi.org/10.1051/0004-6361:20077840)
- Virtanen, P., Gommers, R., Oliphant, T. E., et al. 2020, *Nature Methods*, 17, 261, doi: [10.1038/s41592-019-0686-2](https://doi.org/10.1038/s41592-019-0686-2)
- Wang, T., Yuan, H., Chen, B., et al. 2025, *ApJS*, 280, 15, doi: [10.3847/1538-4365/adea39](https://doi.org/10.3847/1538-4365/adea39)
- Werner, K., Reindl, N., Löbbling, L., et al. 2020, *A&A*, 642, A228, doi: [10.1051/0004-6361/202038574](https://doi.org/10.1051/0004-6361/202038574)
- Winters, J. G., Henry, T. J., Jao, W.-C., et al. 2019, *AJ*, 157, 216, doi: [10.3847/1538-3881/ab05dc](https://doi.org/10.3847/1538-3881/ab05dc)
- Wonnacott, D., Kellett, B. J., & Stickland, D. J. 1993, *MNRAS*, 262, 277, doi: [10.1093/mnras/262.2.277](https://doi.org/10.1093/mnras/262.2.277)
- Yamaguchi, N., El-Badry, K., Ciardi, D. R., et al. 2024a, *PASP*, 136, 074201, doi: [10.1088/1538-3873/ad5ebd](https://doi.org/10.1088/1538-3873/ad5ebd)
- Yamaguchi, N., El-Badry, K., Rees, N. R., et al. 2024b, *PASP*, 136, 084202, doi: [10.1088/1538-3873/ad6809](https://doi.org/10.1088/1538-3873/ad6809)
- Yamaguchi, N., El-Badry, K., & Shahaf, S. 2025, *PASP*, 137, 104205, doi: [10.1088/1538-3873/ae0d30](https://doi.org/10.1088/1538-3873/ae0d30)
- Yamaguchi, N., El-Badry, K., Fuller, J., et al. 2024c, *MNRAS*, 527, 11719, doi: [10.1093/mnras/stad4005](https://doi.org/10.1093/mnras/stad4005)
- Zahn, J. P. 1977, *A&A*, 57, 383
- Zhao, Z.-Q., Li, Z.-W., Xiao, L., Ge, H.-W., & Han, Z.-W. 2024, *MNRAS*, 531, L45, doi: [10.1093/mnras/slae029](https://doi.org/10.1093/mnras/slae029)
- Ziegler, M., Rauch, T., Werner, K., Köppen, J., & Kruk, J. W. 2012, *A&A*, 548, A109, doi: [10.1051/0004-6361/201219536](https://doi.org/10.1051/0004-6361/201219536)